Detecting Nighttime Fire Combustion Phase by Hybrid Application of Visible and Infrared Radiation from Suomi NPP VIIRS

Jun Wang[*] [a,b,c], Sepehr Roudini[*] [a,b,d], Edward J. Hyer [e], Xiaoguang Xu [a,b], Meng Zhou [b,c], Lorena Castro Garcia [a,b], Jeffrey S. Reid [d], David Peterson[e], Arlindo Da Silva[f]

[a] Department of Chemical & Biochemical Engineering, The University of Iowa, Iowa City, Iowa 52242, United States

[b] Center for Global and Regional Environmental Research, University of Iowa, Iowa City, Iowa 52242, United States

[c] Interdisciplinary Graduate Program in GeoInformatics, University of Iowa, Iowa City, Iowa 52242, United States

[d] Now at Department of Economics, The University of Iowa, Iowa City, Iowa 52242, United States

[d] Naval Research Laboratory, Monterey, California 93943, United States

[f] NASA Goddard Space Flight Center, Greenbelt, Maryland 20771, United States

Submitted to Remote Sensing of Environment

March 2019

Major Revision

August 2019

Minor Reivsion

September 2019

Abstract: An accurate estimation of biomass burning emissions is partially limited by the lack of knowledge of fire burning phase (smoldering vs. flaming). In recent years, several fire detection products have been developed to provide information of fire radiative power (FRP), location, size, and temperature of fire pixels, but no information regarding fire burning phase is retrieved. The Day-Night band (DNB) aboard Visible Infrared Imaging Radiometer Suite (VIIRS) is sensitive to visible light from flaming fires in nighttime scenes. In contrast, VIIRS 4 μm moderate resolution band #13 (M13), though capable of detecting fires at all phases, has no direct sensitivity for discerning fire phase. However, the hybrid usage of VIIRS DNB and M-bands data is hampered by their different scanning technology and spatial resolution. In this study, we present a novel method to rapidly and accurately resample DNB pixel radiances to the footprint of M-band pixels, accounting for onboard detector aggregation schemes and bowtie effect removals. The visible energy fraction (VEF) is subsequently introduced as an indicator of fire burning phase VEF is calculated as the ratio of visible light power (VLP) to FRP for each fire pixel retrieved from the VIIRS 750 m active fire product. A global distribution of VEF values, and thereby the fire phase, is quantitatively obtained, showing smaller VEF values in regions with mostly smoldering wildfires, such as peatland fires in Indonesia, larger VEF values in regions with flaming wildfires over grasslands and savannas in the sub-Sahelian region, and the largest VEF values associated with gas flaring in the Middle East. Mean VEF for different land cover types or regions is highly correlated with modified combustion efficiency (MCE). These results, together with a case study of the 2018 California Camp Fire, show that the VEF has the potential to be an indicator of fire combustion phase for each fire pixel, appropriate for estimating emission factors at the satellite pixel level.

Keywords: fire combustion phase, flaming or smoldering, Visible Infrared Imaging Radiometer Suite (VIIRS), Day–Night band (DNB), area-weighting, pixel size, wildfire

1. Introduction

Biomass burning has a significant role in Earth's atmosphere and climate system. On average, 348 Mha of land is burned by wildfires and prescribed fires worldwide each year (Giglio et al. 2013). These fires emit radiatively important greenhouse gases (including their precursors) into the atmosphere, such as carbon dioxide (CO_2), carbon monoxide (CO), nitrous oxide (N_2O), and methane (CH_4), along with smoke particles with significant apportionments of black carbon (BC) and organic carbon (OC) (Andreae and Merlet 2001; Ichoku and Ellison 2014; Ichoku and Kaufman 2005). Such greenhouse gases and smoke particles disturb atmospheric radiative balance by scattering and absorbing solar radiation, which can affect climate and air quality regionally and globally (Kaufman et al. 1991; Penner et al. 1992; Ramanathan and Carmichael 2008; Wang and Christopher 2006b). While greenhouse gases have a positive radiative forcing effect from absorbing the Earth's longwave radiation and emitting it back to the surface, smoke aerosol particles can produce a radiative cooling effect by scattering and absorbing incident solar radiation before it reaches the surface (Wang and Christopher, 2006).

While qualitatively understood, the overall impact from biomass burning on climate and air quality remains highly uncertain due to discrepancies in the estimation of biomass burning emission amount and the OC/BC ratio that regulates the single scattering albedo of the smoke particles. For example, Ge et al. (2014) conducted a WRF-Chem simulation using different OC/BC ratios in smoke emissions, and showed that the smoke direct radiative forcing increases by a factor of 2 as the OC/BC ratio changes from 10 to 3.5. Feng et al. (2014) showed that the estimation for monthly-total smoke (OC + BC) emissions from 9 different inventories can differ by a factor of 12 over northern sub-Saharan Africa (15°W–42°E, 13°S–17°N). These studies highlight the

1 importance of OC/BC ratio for both radiative forcing calculations and for resolving (at least
2 partially) the discrepancies of the total emission of OC and BC in emission inventories.
3 Most emission inventories use constant emission factors (EF, grams of greenhouse gas or
4 particulate matter emitted per kilogram of burned dry matter) for each vegetation type to estimate
5 the emissions for any wildfire. This formulation is an oversimplification because emission factors
6 are dependent on the fire combustion efficiency (CE, the ratio of carbon emitted as CO_2 to the total
7 carbon emitted) that in turn varies with fire combustion phase and can vary highly with space and
8 time, even in the same region for the same fuel type (Akagi et al. 2011; Reid et al. 2005). A higher
9 value of CE (e.g., ≥ 0.9) generally coincides with the flaming phase, when the biomass fuel load
10 burns with flames emitting mostly CO_2, H_2O, and NO_X. Flaming fires at high temperatures can
11 also produce BC. In contrast, lower values of CE (e.g., < 0.9) are primarily due to the smoldering
12 phase of fire, resulting in a decrease in the emission of CO_2 accompanied by an increase in the
13 emission of CO and OC aerosol (Ward and Hardy 1991; Yokelson et al. 1996). It is therefore
14 important to develop techniques to characterize the spatiotemporal variation of fire combustion
15 phase from satellite sensors.
16 Global monitoring of fires became a reality with the advent of operational polar-orbiting
17 and geostationary weather satellites in the 1970s. A wide variety of sensors have been used to
18 monitor fires, including Advanced Very High Resolution Radiometer (AVHRR) (Dozier 1981),
19 the Defense Meteorological Satellite Program (DMSP) Operational Linescan System (Elvidge et
20 al. 1996), the Along-Track Scanning Radiometer (ATSR) (Mota et al. 2006), the Visible and
21 Infrared Scanner (VIRS) (Giglio et al. 2000), the Moderate Resolution Imaging Spectroradiometer
22 (MODIS) (Kaufman et al. 1998), the Visible Infrared Imaging Radiometer Suite (VIIRS) (Csiszar
23 et al. 2014; Schroeder et al. 2014), the Geostationary Operational Environmental Satellite (GOES)

Imager (Prins and Menzel 1992, 1994) and the Spinning Enhanced Visible and Infrared Imager (SEVIRI) (Roberts et al. 2005; Roberts and Wooster 2008). By employing top-of-atmosphere radiances measured in several wavelengths, many fire detection algorithms have been developed for these sensors to characterize wildfires. In the absence of solar contamination during the night, specific algorithms for nighttime fire detection using short-wave infrared band (SWIR) centered near 1.6 μm (Elvidge et al. 2013) and visible-light band centered near 0.7 μm (Polivka et al. 2016) were demonstrated for VIIRS onboard the Suomi National Polar-orbiting Partnership (S-NPP) satellite. The detailed specifications for each fire detection algorithm can be found in Table 1. While significant progress has been made toward detecting and characterizing active wildfires using remote sensing satellite data, there is no quantitative characterization of fire combustion phase in these satellite-based active fire products. The goal of this study is to develop a technique that measures fire combustion phase from space using nighttime satellite remote sensing data, thereby providing a potential means to improve fire emission estimation, with a specific focus on emission factors for each individual fire.

Fire combustion phase is dependent on fuel content, relative humidity, and temperature, which define the nature of the combustion reaction. If the reaction happens heterogeneously at the surface of solid fuels (vegetation and wood), the combustion is without flames and produces incompletely oxidized products (Ohlemiller 1985; Rein 2009). In contrast, when the oxidation happens between oxygen in the air and gases released by pyrolysis, the combustion products are soot and completely oxidized gases. These products absorb substantial energy during the combustion process, allowing them to emit visible radiation as a flame (Rein 2009; Sato et al. 1969). Combustion efficiency is usually reported as modified combustion efficiency (MCE), which is defined as the ratio of carbon emitted as CO_2 to the total carbon emitted as CO_2 and CO.

In fire emission inventory estimates, EF is normally defined as a function of MCE. Although MCE can be identified through lab or in-situ measurements (Akagi et al. 2011; Ferek et al. 1998; Ward and Hardy 1991), it is difficult to determine MCE, and therefore EF, on a near real-time basis in an open environment, where both flaming and smoldering occur simultaneously (van Leeuwen and van der Werf 2011; Ward and Hardy 1991). This results in a lack of availability of MCE data for fires observed routinely and globally.

This study is the first attempt to use VIIRS observations for characterizing the dominant fire combustion phase quantitatively and globally, with a link to the fire CE, from which the emission factors for BC and OC can be derived for a given surface type and an individual fire. In section 2, we illustrate the VIIRS Day-Night band (DNB) and moderate-resolution band (M-band) characteristics, and their spatial mismatch problem at the pixel level. In section 3, we present the methodology to efficiently collocate DNB pixel radiances to M-band pixel resolution. This is required because DNB and M-bands have significant differences in their sampling and scan geometry. Once DNB and M-band data are homogenized, we describe a method to retrieve a visible energy fraction (VEF) for each fire pixel, and link that VEF to the emission factors that are used worldwide to initialize smoke transport and air quality forecasts. Section 4 presents results for several fire classifications based on their VEF values, including a global distribution of fire combustion phase and the first global fire combustion efficiency map for the year 2015. Section 5 concludes the paper.

2. VIIRS: M-band and DNB spatial mismatch and Data Used

VIIRS is a remote-sensing instrument flying on the S-NPP and NOAA-20 (also referred to as JPSS-1) satellite platforms. NOAA-20 is the first in a new series of polar-orbiting environmental

satellites, called the Joint Polar Satellite System or JPSS, created in partnership between the National Oceanic and Atmospheric Administration (NOAA) and National Aeronautics and Space Administration (NASA). VIIRS will be flown onboard three more satellites (JPSS-2, JPSS-3, JPSS-4) to be launched in the next 10-15 years (Goldberg et al. 2013).

VIIRS has 22 channels, with a nominal spatial resolution of 375 m in the five imagery bands (I-bands) and 750 m in 16 moderate resolution bands (M-bands), covering a spectral range from 0.412 μm to 12.01 μm (Table S1). Included on VIIRS is the unique DNB that measures radiances over a broadband spectrum from 0.4 to 0.9 μm (Cao et al. 2014; Wolfe et al. 2013). DNB minimum detectable radiance (L_{min}) is 3×10^{-9} $W\cdot cm^{-2}\cdot sr^{-1}$ during the night, which coincides with a temperature near 630 K for a fire occupying half of the pixel (Fig. 1a), to a maximum value of 0.02 $W\cdot cm^{-2}\cdot sr^{-1}$ in the presence of sunlight. Fig. 1a shows atmospherically corrected DNB radiances for different fire temperatures and fractions. We assumed the night to be moonless, and did not take into account any moon effect in our simulation. The simulation was conducted by the Unified Linearized Vector Radiative Transfer Model (UNL-VRTM) (Wang et al. 2014) for each fire pixel with a surface temperature of 300 K and a uniform background aerosol optical depth near 0.1 (smoke particles, wavelength = 0.75 μm). The black line represents L_{min} for the DNB. Furthermore, as Fig. 1b shows, DNB has a broad spectral response with a high dynamic range, which is sensitive to flaming fire temperatures exceeding 600 K. VIIRS DNB radiances therefore contain strong unsaturated signal from fire flames during nighttime, in the absence of significant background solar contamination.

The VIIRS 750 m active fire (AF) product provides information on active fires and FRP. The VIIRS AF algorithm almost exclusively builds on the MODIS fire detection algorithm, which is based on multi-spectral tests using the infrared channels (Giglio et al. 2016). Also, the VIIRS

AF algorithm derives FRP based on the VIIRS 4 μm moderate resolution band #13 (M13) radiance using the method proposed by Wooster et al. (2005). However, to obtain visible light information for a fire pixel detected by infrared M-band, it is necessary to ensure that DNB pixels are properly matched to the M-band pixels. This matching is complicated by the fact that DNB and M-bands are completely different in their mechanics and operations. Subsequent sections describe these fundamental differences between DNB and M-bands in their manners to collect the observations and their procedures for aggregating samples observed by individual detectors to form pixels. This is followed by a description of DNB and M-band mismatch and the data products used for this study.

2.1. M-band and DNB differences in onboard processing

Each M-band has 16 detectors, and consequently, each of the M-band scans is comprised of 16 scan lines. Hereafter, the region consisting of these detector lines in one M-band scan is referred to as one scan zone. The M-bands use a whiskbroom procedure, scanning the earth perpendicular to the track of the satellite (Cao et al. 2014; Polivka et al. 2015; Polivka et al. 2016; Wolfe et al. 2013). The whiskbroom scanning causes the pixel size to grow as the scan angle increases, producing the so-called "bowtie effect". This pixel size growth occurs in both the along-scan and along-track directions, but it is larger in the along-scan direction. The bowtie effect causes some of the scan lines in two consecutive scan zones to overlap each other far from nadir, resulting in redundant sampling. For example, for the M-band, the last 9 scan lines in the first scan zone overlap with the first 9 scan lines in the next scan zone, as shown in Fig. 2a. The resulting overlapped region is partially flagged onboard and removed by trimming 4 overlapped scan lines (2 from each scan zone) at the edge of the scan zone (corresponding with a scan angle around

56.28°). However, 5 additional scan lines not removed by the onboard bowtie deletion remain overlapped near the edge of each scan.

In addition to the bowtie effect, within each scan zone, there are three symmetrical aggregation zones for M-bands on each side of the scan zone (Table S2) (Polivka et al. 2015). Within the M-band field-of-view, each scan line has 3200 pixels after aggregation of 6304 detector pixels, and each M-band's detector samples a distance of 259 meters along the scan and 742 meters across the scan at the nadir on the earth's surface. The aggregation zones for the left side of the scan zone are denoted by blue dashed lines in Fig. 3. In aggregation zone 3:1 (scan angles between 0˚and 31.59˚), 3 consecutive samples (detector footprints) made by individual detectors along the scan are aggregated to comprise one pixel that has a size of 776 (259×3) meters along the scan and 742 meters across the scan at the nadir. In aggregation zone 2:1 (scan angles between 31.59˚ and 44.68˚), two consecutive samples from each detector along the scan line comprise one pixel. In aggregation zone 1:1 (scan angles larger than 44.68˚), no aggregation happens as the along-scan growth in size makes each sample large enough as a square-like pixel. Without aggregation, the ground footprint of the VIIRS detectors grows by a factor of 6 from nadir to the edge of the scan. Because of the detector aggregation scheme, pixel footprints grow by only a factor of 2 across the scan, and the width and length of the pixel are similar throughout the scan zone.

While a similar aggregation strategy is applied, DNB uses charge-coupled device (CCD) arrays with 672 detectors in the along-track direction and a larger number in the along-scan direction (Liao et al. 2013). This 2-D detector array permits aggregating samples retrieved from detectors both along and across the scan. Contrary to M-band, DNB has 32 symmetrical aggregation schemes on each side of the scan (Table S3) to keep the similar pixel size (742 m) throughout the whole scan. In Fig. 3, the bumps in DNB lines indicate the start of a new

aggregation zone, which has a different number of aggregated samples in the across-scan direction than that of the adjacent aggregation zones. The unique aggregating scheme in DNB also removes the bowtie effect (or the pixel area overlap) completely. Consequently, DNB pixels have approximately the same size throughout the whole scan, while M-band pixels are affected by the bowtie effect.

2.2. M-band and DNB mismatch

As a result of the DNB and M-band on board processing and formulation differences, two kinds of mismatch exist between VIIRS M-band and DNB pixels, even though their respective scan zone covers the same portion of the area in the VIIRS ground swath. The first type of mismatch is due to the difference between the nominal spatial resolution of the DNB and M-band pixels at nadir. As Fig. 3a shows, M-band and DNB nadir pixels match perfectly in the along-track direction (Y direction), where the top and bottom sides of the pixels overlap each other. The left and right sides of the pixels in the along-scan (X) direction do not match exactly, rendering a small offset for the same nadir location in the same scan line.

The second kind of mismatch between M-band and DNB pixel footprints results from divergence in pixel size growth arising from the different methodologies for treating the bowtie effect. This mismatch is denoted by arrows (offset 1 and offset 2) for edge pixels in Fig. 3, where only 8 scan lines (in the center) of the M-band scan zone are fully within the DNB scan zone, and fully overlap with the 16 DNB scanlines in the same DNB scan zone. The remaining 8 M-band scan lines are completely outside of the DNB scan zone at the edge, despite having full overlap with those DNB scan lines at the nadir. Hence, an M-band pixel at the scan edge can overlap with up to 12 DNB pixels spreading over four adjacent DNB scan lines (Fig. 3b).

The DNB and M-band mismatch hinders the combined use of valuable DNB radiance with M-band radiances for fires that require precise georeferencing for the exact same fire area. However, since both the DNB and M-bands cover the same swath for the same scan zone at the nadir, and their mismatch pattern is repeatable for each scan zone, it is possible to collocate DNB to M-band for one scan zone, and save the results to produce a look-up table that can be applied to any other scan zone (as described in section 3).

2.3. Data Used

To implement DNB to M-band collocation, we obtained the VIIRS Suomi NPP data including M-band geolocation product (VNP03MOD) and DNB geolocation product (VNP03DNB) from the NASA level-1 and atmosphere archive & distribution system (LAADS) (https://ladsweb.modaps.eosdis.nasa.gov/). We also obtained the Level-1 B calibrated DNB radiance product (VNP02DNB) and VIIRS 750 m active fire (AF) product (VNP14) (Csiszar et al. 2014) from LAADS for 2017 (only nighttime). Fig. S1 in supplementary material shows the global distribution of nighttime fire pixels for 2017. We obtained dominant vegetation type information from the MODIS Land Cover Type Climate Modeling Grid (0.05˚) product (Short Name: MCD12C1) (Friedl et al. 2010), which is obtained from land processes distributed active archive center (LP DAAC) (https://lpdaac.usgs.gov/). MCD12C1 uses the International Geosphere-Biosphere Program (IGBP) classification stratifying the earth's surface cover into 17 categories.

We obtained gas flare location data from the VIIRS Nightfire flares only product (Elvidge et al. 2016), produced from image and data processing by NOAA's national geophysical data center

(https://ngdc.noaa.gov/) to classify flare-type grids. Fig. S2 in supplementary material shows the gas flare locations that are used in this study.

We use the global fire emissions database version 4 (GFED4) (https://www.globalfiredata.org/) (van der Werf et al. 2017) data to calculate MCE ($= \frac{CO_2}{CO_2+CO}$) for each GFED4 grid (0.25˚). GFED4 reports monthly emission estimation (grams) of different trace gases like CO and CO_2 for different vegetation types for the globe, based on emission factors from Akagi et al. (2011). GFED4 also provides these estimations for 14 basis regions. This dataset is used as an independent check of the results from our algorithm (described in subsequent sections).

2.4. Data Processing

We extract FRP data from VIIRS AF for all detected nighttime fire pixels (having a solar zenith angle greater than 85˚) for 2015 and 2017 globally. When repeating the analysis including only fire pixels with a confidence level exceeding 50%, the results are nearly identical. Consequently, we include all detected fire pixels in our analysis. We then use the collocation algorithm to obtain the collocated DNB radiance and calculate VEF for each of those (M-band) fire pixels. We can regrid the pixels into various grid resolutions, depending on the application. For example, for characterizing VEF over different surface cover types, we regrid VEF pixel data into MODIS land cover type grids (0.05˚). To compare VEF with MCE, we use GFED4 grids (0.25˚). We also regrid VEF pixel values into 1˚ grids to provide a global map. Furthermore, to generate a global and anuual map, we only use the grids with at least 5 fire pixels and report annual-averaged VEF for each grid by averaging pixel VEF values in each grid.

We employ VEF to investigate nighttime fire combustion phase based on the different MODIS IGBP land cover types (Fig. 9b, Table 2) and gas flares (Fig. S2). Note, we consider MODIS savannas and woody savannas as one land cover type (savannas), and open/closed

shrublands as general shrublands. Furthermore, we show the capability of VEF to characterize fire combustion phase by correlating it to the MCE values derived from GFED4 2015 emission data for 14 GFED4 basic regions (Fig. 4a) as well as six GFED4 general biomes, plus the gas flares (we assume gas flaring MCE to be 0.99 as the gas flares are mostly comprised of flames). We reclassify the MODIS land cover types into the broad vegetation types that are used by GFED4 for reporting emission factors (Akagi et al. 2011) and dry matter emissions (Table 2). In this way, we can compare and correlate VEF and MCE for the same biomes. However, while peat is one of the biomes used by GFED4, the MODIS land cover product does not provide peatland locations. We therefore identify peatland grids by deriving the fraction of peat vegetation from each GFED4 grid (0.25˚); if more than 70% of a grid land cover is peat, we classify it as peatlands, which are located at regions of Sumatra and Kalimantan (Fig. 4b). In 2017 (primary analysis year), there were not enough fire pixels in these peatland grids, resulting in inadequate VEF information for peats. Consequently, we use the 2015 VIIRS AF data because of a large peatland fire event observed in Indonesia (Huijnen et al. 2016), providing a sufficient quantity of valid peatland grids to retrieve a reliable VEF for the peat vegetation type. Finally, we illustrate how VEF can identify intensity changes during the lifetime of a major wildfire by analyzing the 2018 Camp Fire in California.

3. Algorithm

3.1. Collocating *DNB to M-band*

The principle of collocation is to aggregate different DNB pixels into the M-band resolution by assigning them different weights according to their respective area and the corresponding M-band pixel area. We collocate DNB to M-band for a scan using area-weighting, so the energy is conserved in the collocation process. We choose a scan specifically near the

equator that has minimal curvature effect to reduce errors in calculating areas of pixels. The collocation process is summarized as a flow chart in Fig. 5.

The first step of the collocation algorithm splits one scan zone of DNB in the along-scan direction (X-axis) into smaller segments called collocation segments, allowing the collocation process to be implemented separately for each of these small segments to reduce distortion errors. We use the DNB aggregation zones as our index for collocation segments. If two consecutive aggregation zones utilize the same number of detector samples in the track direction for aggregation (as described in section 2.1), they will be assumed as a single collocating segment because the pattern along the scan will remain consistent (Fig. 3). There are 64 aggregation zones for one DNB scan zone (32 on each side of nadir), which comprises 46 collocation segments (23 on each side). The details of the pixel ranges for each collocation segments are provided in Table S4.

Second, for each collocation segment, pixels are projected onto the earth's surface and the projected pixels centroids are used to calculate each pixel corners and area. The Albers equal area projection method is used to project pixel lat/lon coordinates to a flat surface because it is appropriate for satellite swath data as the distortion is minimal in east to west direction in the scan zone (Yildirim and Kaya 2008). This flat surface is a two-dimensional coordinate system where the horizontal axis (X-axis) corresponds with the projected longitude and the vertical axis (Y-axis) represents the projected latitudes in meters. The origin point (X=0, Y=0) of the flat surface corresponds with the lower left pixel in the collocating segment. Fig. S3 shows the projected DNB and M-band pixels comprising collocation segment 7.

The third step of the algorithm identifies the overlapped DNB pixels intersecting with each M-band pixel in the scan zone of DNB and calculates their area weights. This step is applied to all

M-band pixels in each collocation segment. We denote the given M-band pixel as $M_{i,j}$, where the subscript i shows the scan line (from 1 to 16) and j is the number of pixels along that scan line (from 1 at nadir to 3200 at edge). Similarly, a DNB pixel is denoted as $D_{l,k}$ where l is the scan line (from 1 to 16) and k is the pixel number (from 1 to 4064). As shown in Fig. 6, x_{MLR} and x_{DLR} represent the pixel lower-right X coordinates of $M_{i,j}$ and $D_{l,k}$ along the scan (in meters), while x_{MLL} and x_{DLL} are the lower-left X coordinates along the scan. Similarly, y_{MUL} and y_{DUL} are the upper-left Y coordinates (along Y axis) of $M_{i,j}$ and $D_{l,k}$ across the scan in meters, while y_{MLL} and y_{DLL} are the lower-left coordinates of each pixel. The $D_{l,k}$ is intersected with $M_{i,j}$ if:

$$\Delta X = Min(x_{MLR}, x_{DLR}) - Max(x_{MLL}, x_{DLL}) > 0 \quad (1)$$

$$\Delta Y = Min(y_{MUL}, y_{DUL}) - Max(y_{MLL}, y_{DLL}) > 0 \quad (2)$$

where the minimum of the two coordinates denotes the smaller coordinate value, while maximum means the larger coordinate value. Once the intersection is detected, the ratio of the intersected area of DNB pixel to M-band pixel area, which is the area weight, is calculated as follows:

$$S_{i,j}^{M} = (x_{MLR} - x_{MLL}) \times (y_{MUL} - y_{MLL}) \quad (3)$$

$$s(D_{l,k}, M_{i,j}) = \Delta X \times \Delta Y \quad (4)$$

$$W(D_{l,k}, M_{i,j}) = \frac{s(D_{l,k}, M_{i,j})}{S_{i,j}^{M}} \quad (5)$$

where $S_{i,j}^{M}$ is the $M_{i,j}$ pixel area and $s(D_{l,k}, M_{i,j})$ is the area that $D_{l,k}$ intersected with $M_{i,j}$. The weight of $D_{l,k}$ for $M_{i,j}$ is denoted by $W(D_{l,k}, M_{i,j})$. After we calculate the DNB area weights, the collocated DNB radiance can be calculated as follows:

$$R_{M_{i,j}}^{D} = \sum_{l,k} W(D_{l,k}, M_{i,j}) \times R_{l,k}^{D} \quad (6)$$

where $R^{D}_{M_{i,j}}$ is the DNB radiance for $M_{i,j}$ and $R^{D}_{l,k}$ is the radiance retrieved from the intersected DNB pixel ($D_{l,k}$). It should be noted that the sum of the intersected DNB pixels weights will add up to 1 ($\sum_{l,k} W\ (D_{l,k}\ , M_{i,j}\ ) = 1$) for each $M_{i,j}$ that is completely overlapped with DNB pixels.

We store the index of each M-band pixel and its corresponding intersected DNB pixels indices and weights as a collocation look-up table (LUT). Also, we add the M-band pixel areas to the pixel-area LUT for later use. The collocation LUT details are presented in Supplementary Material Section 1. These LUTs can be applied to any other scan zone because satellite scan zone characteristics, such as pixel areas or pixel size growth pattern are inherent and do not change for different scan zones. For example, a near-equator scan zone's pixel areas are nearly identical for a scan zone in polar regions. Furthermore, the area-weighted collocation method can be applied to any other data with different spatial footprints that need to be resampled to each other. The resampling process for an M-band granule (consists of 3232 scan lines) by applying collocation LUT takes around 3 seconds (using an inexpensive laptop), while it can take up to hours implementing the resampling process without using LUT. The resampled DNB radiances for M-band pixels provide the capability to characterize fire combustion efficiency for each nighttime fire pixel.

3.2. M-band bowtie effect and pixel overlap removal

We detect M-band bowtie affected pixels that are overlapped on each other from two consecutive scan zones using the same technique described in Section 3.1. We use 50% as the threshold for detecting the overlap; if the two M-band pixels overlap more than 50% of their area, they are labeled as overlapped. However, it is not immediately clear which of the two overlapped pixels is redundant. We therefore sum the DNB weights for each overlapped M-band pixel and remove the M-band pixels that have smaller weights from corresponding DNB pixels in the same

scan zone. For example, near the edge, we detect 9 scan lines that overlap between two consecutive scans (Fig. 2a). According to the edge offset (Offset1 & Offset2) of 8 scan lines between DNB and M-band, the last 4 lines from scan zone 1 and the first 4 lines from the scan zone 2 have no DNB pixel overlap; hence they are labeled as redundant pixels (Fig. 2a). Similarly, although the last overlapped line between two scan zones has DNB signals from both scan zones, the DNB weights from the first scan zone are larger than second scan zone, which results in labeling one more scan line from scan zone 2 as redundant. As a result, we remove the 4 bottommost scan lines from scan zone 1 and the 5 topmost scan lines from scan zone 2 as the redundant pixels (Fig. 2b). We detect all the overlapped pixels along the whole scan zone for two consecutive scans, and store the results as a bowtie LUT.

3.3. Visible Energy Fraction (VEF)

Polivka et al. (2016) showed that VIIRS DNB radiance in the night time can be an indicator of fire combustion phase of smoldering versus flaming. However, no quantitative measurement was presented to quantify the CE. The VIIRS AF product provides fire radiative power (FRP) for each fire pixel, which is an estimate of instantaneous radiative energy from actively burning fires (Csiszar et al. 2014; Kaufman et al. 1998; Peterson et al. 2013; Wooster et al. 2005). We derive visible energy fraction (VEF) to quantitatively measure the flaming/smoldering phase for each fire pixel, which is dependent on both FRP (M-band, AF product) and visible light power (VLP, from DNB).

The VLP (in megawatts) for each fire pixel is calculated as follows:

$$VLP = L_{visible} \times A_{pixel} \times \pi \times 10^{-6} \quad (7)$$

where $L_{visible}$ (in $W \cdot cm^{-2} \cdot sr^{-1}$) is the collocated visible radiance from the fire ($R^{D}_{M_{i,j}}$ as in equation 6), A_{pixel} is the M-band pixel area (in cm^2), π is a mathematical constant

that is approximately equal to 3.14 (in steradians), and 10^{-6} is the unit conversion factor from Watts to megawatts. It should be noted that $L_{visible}$ is not corrected for background contamination (e.g. city lights) or moonlight. For example, the presence of intensive city lights in a fire pixel can result in overestimation of fire radiance. However, most of the wildfires happen in remote areas with almost no background contamination ($L_{visible} \approx 0$). Furthermore, the algorithm for VIIRS AF product that is used in this study detects fire pixels based on the thermal anomaly in the infrared channels, and hence the active fire pixels are not affected by artificial/city light as these light sources do not lead to infrared thermal anomaly (Csiszar et al. 2014). Finally, the reflected radiance from a full moon does not exceed 10 $nW \cdot cm^{-2} \cdot sr^{-1}$ (Román et al. 2018), which is comparable to $L_{visible}$ of only around 3% of fire pixels detected in 2017 (if we assume that all the fire pixels are under full moon condition).

Once the VLP is obtained for the pixel, VEF can be calculated as follows:

$$VEF = \frac{VLP}{FRP} \tag{8}$$

where FRP (in megawatts) is the fire radiative power for the fire pixel. The major uncertainty source for VEF is heavy smoke plumes. Light is more strongly scattered in the visible spectrum (e.g. 0.7 μm) than in the infrared (e.g. 4 μm). Consequently, VLP is more affected than FRP, which means the VEF ratio suffers from underestimation under heavy smoke conditions. We simulate VEF using the UNified and Linerilized Radative Transfer Model (UNL-VTRM, Wang et al., 2004; Xu and Wang, 2019) for different fire temperatures (Table S5) and a smoke optical depth around 0.1.

We compare the simulated VEF with the values obtained from fire pixels in 2017 to determine the approximate dynamic range for VEF. For example, the maximum VEF value (≈ 0.25) in our data belongs to gas flare pixels which is close to the simulated VEF value (≈0.28) for

a temperature of 2400 K. Also, we find that the minimum VEF value ($\approx 2.9 \times 10^{-9}$) in the 2017 fire pixel dataset corresponds with a temperature around 570 K in simulation. This temperature is somewhat lower than the minimum detectable fire temperatures by DNB. Nevertheless, quantification of smoke effect on both DNB and FRP should be conducted by future studies because such effect depends on smoke particle size, index of refraction, particle loading, and their vertical profiles, which is beyond the scope of this study on initial algorithm development.

4. Results

4.1. Resampling DNB radiance to M-band footprint

Fig. 7 a and b show a case of resampling DNB radiances into the M-band pixel resolution by applying the collocation LUT. Before the collocation, the bright DNB radiances distinguishes them from the larger M-band pixel footprint (red rectangles). These pixels were retrieved by VIIRS on 12 December 2017 (10:24 am UTC) over Thomas Fire in California. After collocating the DNB radiances with the M-band pixel footprint, the bright DNB pixels are smoothed over the M-band pixel area, which indicates conservation of energy over the area as a result of the area-weighting resampling (Fig. 7b).

We compare our collocation method results with the nearest-neighbor method, which is commonly used for collocation processes in satellite remote sensing data, by correlating collocated DNB radiances to the brightness temperature values for 852 nighttime fire pixels (Thomas fire) detected by VIIRS AF from 5 December to 12 January 2017 (note the data are at log scale). The corresponding thermal emission (i.e., fire pixel energy) is calculated using the fourth power of 4 μm brightness temperature (BT_4) values. Fig. 7c shows when the collocation is only based on the nearest pixel method (i.e., the nearest DNB pixels to an M-band pixel in the same scan line are

remapped to M-band footprint), the resampled radiances are poorly correlated (R=0.21). When the collocation LUT method is applied, the collocated radiances are more reliable and strongly correlated (R=0.61) with the M-band BT_4^4 values (Fig. 7d).

4.2. Fire combustion phase based on the VEF

Each vegetation type follows a specific combustion phase (smoldering/flaming or a mixture of them) based on its chemical compound, fuel content, relative humidity, and fire temperature. Figure 8 shows that while most fire types have a similar FRP range, their VEF ranges are different from each other. FRP is not capable of detecting fire combustion phase because it dependens on both the fire size and temperuate. FRP values can therefore be the same for a large smoldering fire and a small intense flaming fire (Peterson et al. 2013). In contrast, VEF is a ratio for each fire pixel, representing the portion of the fire radiative energy in the visible spectrum. Therefore, VEF is normalized quanity, has the value in the range from 0 to 1, and its variation is less dependent on fire size and FRP (Fig. S7), and has the potential to dynamically characterize different fire combustion phases as shown in Fig. 8 (note that each point VEF and FRP is an annual-averaged value for a 0.05˚ grid for 2017, and the FRP for each fire pixel is based on VIIRS AF fire product).

Figure 8 shows that VEF values for gas flares are clustered on the top of all other fire types, which is expected because they consist of pure flames. FRP alone cannot separate gas flares from other type of fires. Furthermore, Fig. 8a shows that all the forest land cover types have smaller VEF comparing to savanna, grassland and shrubland, indicating that they have a smaller MCE, which is consistent with the literature (Reid et al. 2005). In Fig 8b, we show the VEF and FRP distributions for only three fire types. This visualization illustrates that although each of the gas flare, shrubland, and evergreen broadleaf forest fire types are clustered in a specific range of VEF,

they can still display significant variation. Fire combustion phase can vary for the same vegetation type due to differences in the fire temperature and relative humidity. These results indicate that VEF has the potential to partially describe variation of fire combustion phase at the level of individual fire pixels.

Figure 8c shows the ln(VEF) probability density function (PDF) for each of the fire types (Table 2). The results are almost identical when plotting these data at the individual pixel level (not gridded) (Fig. S4). Shrubland, grassland, and cropland are spread over a similar ln(VEF) range. The average of VEF values for each MODIS land cover type are shown in Table S6. Shrubland fire type, for example, has a higher probability of flaming because its PDF peaks at a larger ln (VEF) than the other wildfire types. Savanna's PDF covers a wide ln (VEF) range, with a peak around -7 (corresponds to a VEF value of 0.00091). It has a longer tail on the left side of its peak, meaning that it has more fires in the smoldering phase comparing to Shrubland. The forest fires PDFs ranges are lower compared to other fire types, which is consistent with the observation that forests generally burn with lower MCE compared to shrublands or grasslands. Mixed forest fires have a larger peak comparing to the other forest fires peaks. Also, mixed forest has a small peak around -5 (corresponds to a VEF value of 0.0067), which is very high and indicates a dominant flaming fire phase. Finally, gas flares are primarily associated with the highest range of -5.5 to -3.5, which is consistent with dominant flaming combustion.

4.3. VEF Global Distribution

Fig. 9a shows a global map of averaged nighttime VEF (1˚grids) for 2017. We also show the corresponding MODIS global landcover map to better visualize the relationship between land cover types and VEF (Fig. 9c). This display uses 1˚ grids for more sampling data points and better

visualization. However, we also produce these global maps at 0.25˚grid resolution, which yields similar results to maps at 1˚ resolution (Fig. S5). The VEF map shows that savanna regions in Middle America (Consists of Mexico, Central America, Caribbean, Columbia, and Venezuela) have lower VEF when compared to African savanna, which means that they are included in the left tail of savanna's PDF (Fig. 8c). Furthermore, open shrublands in Australia (Fig. 9a zoomed-in subplot) burn mostly with a flaming phase because they have high VEF values. This is a distinguishing characteristic from the evergreen needleleaf forest type in North America, which coincides with low VEF values, indicating the smoldering type. In general, the forest land cover, regardless of specific type, has a lower VEF in comparison to savannas, shrublands, grasslands, and croplands. For example, in South America, the VEF changes from high values to smaller values as biomes transit from grasslands and savannas to evergreen broadleaf forests. The same scenario is seen in Australia, North America, and Africa. Also, the grids with the highest VEF (red shading) mostly correspond with gas flares in Middle East, North Africa, Russia, and Mexico.

In contrast to the VEF, the global map of nighttime averaged FRP (1˚grids) (Fig. 9b) does not distinguish the transitions between different fire types. For example, gas flares are not distinguishable because their FRP range is similar to the other fire types. The FRP spread is similar for shrublands in Australia and evergreen needleleaf forest in North America, while the two land cover types are very different (see zoomed-in subplots). This indicates that, as expected, the main driver of the mean-state VEF for each grid is VLP (as shown in Fig. S6). However, zoomed-in subplots in Fig. S6 show that gas flares are better separated from shrublands in the VEF map because unlike VLP, VEF is not driven by the fire size. For example, Fig. S7 in supplementary material shows cases of fire pixels with large VEF values (larger than 0.2), but not large VLP values. These fire pixels coincide with gas flares in Venezuela, indicating that VEF can rigorously

distinguish between small fires with intense flaming combustion phase and large fires with smoldering combustion phase.

4.4. VEF Comparison with MCE

Although VEF is available for each individual nighttime fire pixel, in-situ measurement data coinciding with the VIIRS nighttime overpass are limited for direct comparison with MCE. As a result, we use GFED4 data, which provides emission estimations of CO and CO_2 at a resolution of 0.25˚. However, the GFED grid-based MCE is derived based on both day and night fire data, which requires an annual-averaged VEF and MCE to obtain a mean-state of each land cover type/region. We calculate annual-averaged VEF for different surface types for 2015, and compared with their MCE values derived from GFED4. We show that ln(VEF) is highly correlated (R=0.89) with MCE for different biomes (Fig. 10a). Furthermore, Fig. 10b shows that the regional averaged VEF and MCE are correlated with each other confirming the strength of VEF in capturing the fire combustion phase. These results suggest that VEF is a strong indicator for fire MCE based on the fire type and combustion conditions (e.g. relative humidity). In other words, GFED-based MCE can be estimated for each nighttime fire pixel on a near real-time basis by taking advantage of its linear relationship with VEF:

$$MCE = 0.016 \times \ln(VEF) + 1.061 \quad (9)$$

However, it should be noted that the MCE calculated from equation 9 includes errors/uncertainties from both GFED and VEF sources, and it is simply an initial step toward improving emission estimations on a near real-time basis. Furthermore, in terms of the best fit equation, the MCE-VEF relationship derived based on biome types (Fig. 10a and equation 9) is similar to that derived based on the regional averages (Fig. 10b, $MCE = 0.018 \times \ln(VEF) + 1.077$), suggesting this relationship is statistically robust.

Figure 11 shows the global map of MCE for 2017. Each grid value is computed from the pixel VEF values linked to the MCE by equation 9. As expected, gas flares have the highest MCE while the peatlands have the lowest values. Our result (Fig. 11) is consistent with the MCE map presented by van Leeuwen and van der Werf (2011) (Fig. S8), which is based on a multivariate regression equation that incorporates different environmental variables (e.g. fraction tree cover, precipitation, and temperature) to better capture the spatiotemporal variability in GFED based MCE. For example, both maps show that tropical forests correspond with lower MCE values when compared to savannas/shrublands. Also, the transition from African grasslands to savannas shows a decrease in MCE in both maps. The same approach (equation 9) can be applied to the VEF of each pixel VEF to obtain MCE and subsequently used as a dynamica constraint for emission factors for each pixel. For example, the CO_2 emission factor for a specific biome can be adjusted based on its MCE, as higher MCE (VEF) indicates an increase in CO_2 emission factor as the fire burns in flaming phase, emitting larger amounts of CO_2. VEF is advantageous because it is retrieved from satellite data while the fire is active, appropriate for improving emissions estimations.

4.5. Camp Fire

On 08 November 2018, the Camp Fire ignited in Butte County, Northern California. It is currently the deadliest (86 fatalities) and most destructive (US$ 16.5 billion damage) wildfire in California history. According to the California department of forestry and fire protection reports, the Camp Fire burned an area of around 153,336 acres before it was fully contained on 25 November, with the help of rain. We show the fire growth over time using all the nighttime VIIRS fire pixels in Fig. S9. The most intense phase of the fire occurred during the first four days, when strong wind speeds facilitated rapid fire growth, resulting in a fire that burned more than 110,000

acres and destroyed the town of Paradise (www.fire.ca.gov). The Camp Fire therefore provides an ideal case study for investigating VEF, and its capability of capturing the variation in wildfire intensity throughout its lifetime.

As Fig. 12a shows, the VEF (daily-averaged for nighttime fire pixels) was largest (highly flaming) during the first 4 nights of the fire and then started to reduce. This is consistent with the fact that fire was most destructive during the first four days. Fig. S10 shows both VLP and FRP can affect VEF for the fire pixels. Note that the fire ignited on 08 November around 6.33 am local time, so the first satellite nighttime observation was on 09 November. This precludes analysis of the daytime period on 08 November, when some of the most extreme fire spread was observed. The VEF (nighttime) increased from lower values (10 November) to higher values (11 November) for fire pixels in the same areas on the ground (Fig.12 c, d), which is consistent with daily-averaged observations of relative humidity and wind speed (Fig. 12b). We obtained these data from Openshaw station (shown as white star in Fig. S9), located within 12 miles of the fire. This station is part of the Wildland Fire Remote Automated Weather Stations (RAWS) network provided by Western Regional Climate Center (https://raws.dri.edu/). These ground observations show that wind speed increased from 3 m s^{-1} to 7 m s^{-1} and relative humidity decreased from 50% to 25% from 10 to 11 November. The dry air and high wind speeds on 11 November provided favorable conditions for a flaming fire, which explains why VEF increased by a factor of 4 and was the largest on 11 November. Interestingly, FRP on November 11 was only the second largest. Overall, during 09-12 November, both meteorological data (Fig. 12b) and VEF (Fig. 12 a, c, and d) indicate that the fire grew to a more flaming phase during 11 November, which is not observable in the FRP time series (Fig. 12a), highlighting the limited capability of FRP to capture meaningful changes in fire behavior through its lifetime.

The dry conditions and strong wind speeds observed on 11 November were driven by a northeasterly shift in low-level wind direction, which initiated a downslope wind event from the Sierra Nevada Mountains into the Central Valley of California. These winds (locally referred to as "Diablo Winds") compress, dry, and warm the air mass as it flows downhill, supporting extreme fire behavior. Figure S11 provides 700 hPa synoptic chart charts at 18 UTC (10 AM local time) for 08 to 11 November, highlighting the wind shift to northeasterly downslope flow between 10 (Fig. S11b) and 11 (Fig. S11c) November. Similar meteorology supported ignition and the initial period of extreme fire spread on 08 November. After 11 November, the synoptic wind flow shifted to a more typical westerly or northwesterly direction, resulting in increased relative humidity and light winds (Fig. 10b), which do not support extreme fire behavior.

5. Discussion and conclusions

VIIRS DNB provides broadband visible radiance for each pixel. When there is a fire present in the pixel during the night, this radiance contains information/signal from the flames of the fire (assuming no background contamination). The VIIRS fire product is based on the M-band (or I-band), which has a different pixel footprint from DNB. This means that the DNB radiance cannot be applied directly to the VIIRS fire pixels. This study developed an algorithm for collocating VIIRS DNB radiances to the M-band pixel footprint, which employs the hybrid use of all available data from DNB and M-bands. The collocated visible radiance facilitated the development of a ratio representing the visible fraction of the fire energy, which provides a quantitative measure of fire combustion phase.

The collocation algorithm is based on an efficient area-weighting method. By taking advantage of the fixed alignment between DNB and M-band pixels in every VIIRS scan, our LUT-based approach can be applied to any VIIRS granule across the globe. This methodology also

provides a reliable criterion to determine whether to keep or exclude an M-band pixel in the case of the redundant M-band pixels, which are overlapped from two consecutive scans due to along-scan pixel growth size. Results show that our collocation method is more reliable than the nearest-neighbor method, producing a much stronger correlation between the collocated DNB radiances and the corresponding M-band pixel BT_4^4 (the fire pixel energy) values for 852 nighttime VIIRS fire pixels detected during the California Thomas Fire.

We used the resampled DNB radiance to develop a parameter for visible light power (VLP), which approximates the energy from fire flames for each pixel during nighttime observations. Its ratio with FRP yields the visible energy fraction (VEF) of the pixel. VEF theoretically should be able to provide a quantitative measure of the fire combustion phase (smoldering/flaming). Sources of uncertainty for VEF include background contamination (e.g. moon effect and city lights) and light attenuation by thick smoke plumes. Although the moon effect is small, intense city lights and thick smoke plumes can result in overestimation and underestimation of VEF, respectively.

Our results show that VEF successfully characterizes mean-state (annual-averaged) combustion phase of fires based on their fuel (vegetation) type at a pixel and grid level. For example, VEF values for gas flares are distributed in a higher range when compared to other land cover types. In contrast, FRP values for all land cover types (including gas flares) are similarly distributed. An initial assessment of VEF showed that annual-averaged values are strongly correlated to the mean-state modified combustion efficiency (MCE, derived from GFED data) for the general biomes used by GFED. This suggests that VEF can be used to predict the GFED-based MCE, which is a key step toward improved emission estimation in future for individual fires based on specific fire characteristics. For example, we applied VEF to calculate GFED-based MCE for

an extreme wildfire event (2018 Camp Fire) at the individual pixel level, and the prelimary results appear to be in good agreement qualitatively with the derivation from meteorology.

Overall, this study has demonstrated the theoretical development of VEF and its potential to measure fire combustion phase. The results of this work motivate future research focused on the application of VEF to improve emission factors for individual pixels. For example, *in situ* MCE obtained from field observations can be linked to VEF calculated for VIIRS pixels if the measurements are coincident with the VIIRS nighttime overpass. Any *in situ* observation of MCE from nighttime fires is essential for quantifying the uncertainty associated with linking VEF to MCE.

Acknowledgments

This research was supported in part by NASA's Applied Sciences Program (grant no. NNX14AG01G, managed by John A. Haynes) and in part by Office of Naval Research (ONR's) Multidisciplinary University Research Initiatives (MURI) Program under the award N00014-16-1-2040. D. Peterson was supported by the Nasa New Investigator Program.

Appendix A. Supplementary data

References:

Akagi, S.K., Yokelson, R.J., Wiedinmyer, C., Alvarado, M.J., Reid, J.S., Karl, T., Crounse, J.D., & Wennberg, P.O. (2011). Emission factors for open and domestic biomass burning for use in atmospheric models. *Atmos. Chem. Phys., 11*, 4039-4072

Andreae, M.O., & Merlet, P. (2001). Emission of trace gases and aerosols from biomass burning. *Global Biogeochemical Cycles, 15*, 955-966

Cao, C., De Luccia, F.J., Xiong, X., Wolfe, R., & Weng, F. (2014). Early On-Orbit Performance of the Visible Infrared Imaging Radiometer Suite Onboard the Suomi National Polar-Orbiting Partnership (S-NPP) Satellite. *IEEE Transactions on Geoscience and Remote Sensing, 52*, 1142-1156

Csiszar, I., Schroeder, W., Giglio, L., Ellicott, E., Vadrevu, K.P., Justice, C.O., & Wind, B. (2014). Active fires from the Suomi NPP Visible Infrared Imaging Radiometer Suite: Product status and first evaluation results. *Journal of Geophysical Research: Atmospheres, 119*, 2013JD020453

Dozier, J. (1981). A Method for Satellite Identification of Surface-Temperature Fields of Subpixel Resolution. *Remote Sensing of Environment, 11*, 221-229

Elvidge, C., Zhizhin, M., Baugh, K., Hsu, F.-C., & Ghosh, T. (2016). Methods for Global Survey of Natural Gas Flaring from Visible Infrared Imaging Radiometer Suite Data. *Energies, 9*, 14

Elvidge, C.D., Kroehl, H.W., Kihn, E.A., Baugh, K.E., Davis, E.R., & Hao, W.M. (1996). *Algorithm for the retrieval of fire pixels from DMSP operational linescan system data. In J. S. Levine (Ed.), Biomass burning and global change: Remote sensing, modeling and inventory development, and biomass burning in Africa*. Cambridge (Massachusetts): MIT Press

Elvidge, C.D., Zhizhin, M., Hsu, F.C., & Baugh, K.E. (2013). VIIRS Nightfire: Satellite Pyrometry at Night. *Remote Sensing, 5*, 4423-4449

Feng, Z., Jun, W., Charles, I., Edward, J.H., Zhifeng, Y., Cui, G., Shenjian, S., Xiaoyang, Z., Shobha, K., Johannes, W.K., Christine, W., & Arlindo da, S. (2014). Sensitivity of mesoscale

modeling of smoke direct radiative effect to the emission inventory: a case study in northern sub-Saharan African region. *Environmental Research Letters, 9*, 075002

Ferek, R.J., Reid, J.S., Hobbs, P.V., Blake, D.R., & Liousse, C. (1998). Emission factors of hydrocarbons, halocarbons, trace gases and particles from biomass burning in Brazil. *Journal of Geophysical Research: Atmospheres, 103*, 32107-32118

Friedl, M.A., Sulla-Menashe, D., Tan, B., Schneider, A., Ramankutty, N., Sibley, A., & Huang, X. (2010). MODIS Collection 5 global land cover: Algorithm refinements and characterization of new datasets, *114*, 168-182

Ge, C., Wang, J., & Reid, J.S. (2014). Mesoscale modeling of smoke transport over the Southeast Asian Maritime Continent: coupling of smoke direct radiative effect below and above the low-level clouds. *Atmos. Chem. Phys., 14*, 159-174

Giglio, L., Descloitres, J., Justice, C.O., & Kaufman, Y.J. (2003). An Enhanced Contextual Fire Detection Algorithm for MODIS. *Remote Sensing of Environment, 87*, 273-282

Giglio, L., Kendall, J.D., & Justice, C.O. (1999). Evaluation of global fire detection algorithms using simulated AVHRR infrared data. *International Journal of Remote Sensing, 20*, 1947-1985

Giglio, L., Kendall, J.D., & Tucker, C.J. (2000). Remote sensing of fires with the TRMM VIRS. *International Journal of Remote Sensing, 21*, 203-207

Giglio, L., Randerson, J., & van der Werf, G.R. (2013). Analysis of daily, monthly, and annual burned area using the fourth-generation global fire emissions database (GFED4). *Journal of Geophysical Research: Biogeosciences, 118*, 317-328

Giglio, L., Schroeder, W., & Justice, C.O. (2016). The collection 6 MODIS active fire detection algorithm and fire products. *Remote Sensing of Environment, 178*, 31-41

Goldberg, M.D., Kilcoyne, H., Cikanek, H., & Mehta, A. (2013). Joint Polar Satellite System: The United States next generation civilian polar-orbiting environmental satellite system. *Journal of Geophysical Research: Atmospheres, 118*, 13,463-413,475

Huijnen, V., Wooster, M.J., Kaiser, J.W., Gaveau, D.L.A., Flemming, J., Parrington, M., Inness, A., Murdiyarso, D., Main, B., & van Weele, M. (2016). Fire carbon emissions over maritime southeast Asia in 2015 largest since 1997. *Scientific Reports, 6*, 26886

Ichoku, C., & Ellison, L. (2014). Global top-down smoke-aerosol emissions estimation using satellite fire radiative power measurements. *Atmos. Chem. Phys., 14*, 6643-6667

Ichoku, C., & Kaufman, Y.J. (2005). A method to derive smoke emission rates from MODIS fire radiative energy measurements. *IEEE Transactions on Geoscience and Remote Sensing, 43*, 2636-2649

Justice, C.O., Giglio, L., Korontzi, S., Owens, J., Morisette, J.T., Roy, D., Descloitres, J., Alleaume, S., Petitcolin, F., & Kaufman, Y. (2002). The MODIS fire products. *Remote Sensing of Environment, 83*, 244-262

Kaufman, Y.J., Fraser, R.S., & Mahoney, R.L. (1991). Fossil Fuel and Biomass Burning Effect on Climate—Heating or Cooling? *Journal of Climate, 4*, 578-588

Kaufman, Y.J., Justice, C.O., Flynn, L.P., Kendall, J.D., Prins, E.M., Giglio, L., Ward, D.E., Menzel, W.P., & Setzer, A.W. (1998). Potential global fire monitoring from EOS-MODIS. *Journal of Geophysical Research: Atmospheres, 103*, 32215-32238

Li, Z., Kaufman, Y., Ithoku, C., Fraser, R., Trishchenko, A., Gilgil, L., Jin, J., & Yu, X. (2001). A review of AVHRR-based fire active fire detection algorithm: Principles, limitations, and recommendations. In F. Ahern, J.G. Goldammer, & C. Justice (Eds.), *Global and Regional Vegetation Fire Monitoring from Space, Planning and Coordinated International Effort* (pp. 199-225)

Li, Z., Nadon, S., & Cihlar, J. (2000). Satellite-based detection of Canadian boreal forest fires: Development and application of the algorithm. *International Journal of Remote Sensing, 21*, 3057-3069

Liao, L.B., Weiss, S., Mills, S., & Hauss, B. (2013). Suomi NPP VIIRS day-night band on-orbit performance. *Journal of Geophysical Research: Atmospheres, 118*, 12,705-712,718

Mota, B.W., Pereira, J.M.C., Oom, D., Vasconcelos, M.J.P., & Schultz, M. (2006). Screening the ESA ATSR-2 World Fire Atlas (1997–2002). *Atmos. Chem. Phys., 6*, 1409-1424

Ohlemiller, T.J. (1985). Modeling of smoldering combustion propagation. *Progress in Energy and Combustion Science, 11*, 277-310

Penner, J.E., Dickinson, R.E., & O'Neill, C.A. (1992). Effects of Aerosol from Biomass Burning on the Global Radiation Budget. *Science, 256*, 1432-1434

Peterson, D., Wang, J., Ichoku, C., Hyer, E., & Ambrosia, V. (2013). A sub-pixel-based calculation of fire radiative power from MODIS observations: 1 Algorithm development and initial assessment. *Remote Sensing of Environment, 129*, 262-279

Polivka, T.N., Hyer, E.J., Wang, J., & Peterson, D.A. (2015). First Global Analysis of Saturation Artifacts in the VIIRS Infrared Channels and the Effects of Sample Aggregation. *IEEE Geoscience and Remote Sensing Letters, 12*, 1262-1266

Polivka, T.N., Wang, J., Ellison, L.T., Hyer, E.J., & Ichoku, C.M. (2016). Improving Nocturnal Fire Detection With the VIIRS Day-Night Band. *IEEE Transactions on Geoscience and Remote Sensing, 54*, 5503-5519

Prins, E.M., & Menzel, W.P. (1992). Geostationary satellite detection of bio mass burning in South America. *International Journal of Remote Sensing, 13*, 2783-2799

Prins, E.M., & Menzel, W.P. (1994). Trends in South American biomass burning detected with the GOES visible infrared spin scan radiometer atmospheric sounder from 1983 to 1991. *Journal of Geophysical Research: Atmospheres, 99*, 16719-16735

Ramanathan, V., & Carmichael, G. (2008). Global and regional climate changes due to black carbon. *Nature Geoscience, 1*, 221

Reid, J.S., Koppmann, R., Eck, T.F., & Eleuterio, D.P. (2005). A review of biomass burning emissions part II: intensive physical properties of biomass burning particles. *Atmos. Chem. Phys., 5*, 799-825

Rein, G. (2009). Smouldering Combustion Phenomena in Science and Technology. *International Review of Chemical Engineering, 1*, 3-18

Roberts, G., Wooster, M.J., Perry, G.L.W., Drake, N., Rebelo, L.M., & Dipotso, F. (2005). Retrieval of biomass combustion rates and totals from fire radiative power observations: Application to southern Africa using geostationary SEVIRI imagery. *Journal of Geophysical Research: Atmospheres, 110*

Roberts, G.J., & Wooster, M.J. (2008). Fire Detection and Fire Characterization Over Africa Using Meteosat SEVIRI. *IEEE Transactions on Geoscience and Remote Sensing, 46*, 1200-1218

Román, M.O., Wang, Z., Sun, Q., Kalb, V., Miller, S.D., Molthan, A., Schultz, L., Bell, J., Stokes, E.C., Pandey, B., Seto, K.C., Hall, D., Oda, T., Wolfe, R.E., Lin, G., Golpayegani, N., Devadiga, S., Davidson, C., Sarkar, S., Praderas, C., Schmaltz, J., Boller, R., Stevens, J., Ramos González, O.M., Padilla, E., Alonso, J., Detrés, Y., Armstrong, R., Miranda, I., Conte, Y., Marrero, N., MacManus, K., Esch, T., & Masuoka, E.J. (2018). NASA's Black Marble nighttime lights product suite. *Remote Sensing of Environment, 210*, 113-143

Sato, T., Kunitomo, T., Yoshii, S., & Hashimoto, T. (1969). On the Monochromatic Distribution of the Radiation from the Luminous Flame. *Bulletin of JSME, 12*, 1135-1143

Schroeder, W., Oliva, P., Giglio, L., & Csiszar, I.A. (2014). The New VIIRS 375m active fire detection data product: Algorithm description and initial assessment. *Remote Sensing of Environment, 143*, 85-96

van der Werf, G.R., Randerson, J.T., Giglio, L., van Leeuwen, T.T., Chen, Y., Rogers, B.M., Mu, M., van Marle, M.J.E., Morton, D.C., Collatz, G.J., Yokelson, R.J., & Kasibhatla, P.S. (2017). Global fire emissions estimates during 1997–2016. *Earth Syst. Sci. Data, 9*, 697-720

van Leeuwen, T.T., & van der Werf, G.R. (2011). Spatial and temporal variability in the ratio of trace gases emitted from biomass burning. *Atmos. Chem. Phys., 11*, 3611-3629

Wang, J., & Christopher, S.A. (2006a). Mesoscale modeling of Central American smoke transport to the United States, Part II, smoke radiative impact on regional surface energy budget and boundary layer process. J. Geophys. Res., 111, D14S92, doi:10.1029/2005JD006416

Wang, J., & Christopher, S.A. (2006b). Mesoscale modeling of Central American smoke transport to the United States: 2. Smoke radiative impact on regional surface energy budget and boundary layer evolution. Journal of Geophysical Research: Atmospheres, 111

Wang, J., Xu, X., Ding, S., Zeng, J., Spurr, R., Liu, X., Chance, K., & Mishchenko, M. (2014). A numerical testbed for remote sensing of aerosols, and its demonstration for evaluating retrieval synergy from a geostationary satellite constellation of GEO-CAPE and GOES-R. Journal of Quantitative Spectroscopy and Radiative Transfer, 146, 510-528

Ward, D.E., & Hardy, C.C. (1991). Smoke emissions from wildland fires. Environment International, 17, 117-134

Wolfe, R.E., Lin, G., Nishihama, M., Tewari, K.P., Tilton, J.C., & Isaacman, A.R. (2013). Suomi NPP VIIRS prelaunch and on-orbit geometric calibration and characterization. Journal of Geophysical Research: Atmospheres, 118, 11,508-511,521

Wooster, M.J., Roberts, G., Perry, G.L.W., & Kaufman, Y.J. (2005). Retrieval of biomass combustion rates and totals from fire radiative power observations: FRP derivation and calibration relationships between biomass consumption and fire radiative energy release. Journal of Geophysical Research: Atmospheres, 110

Yokelson, R.J., Griffith, D.W.T., & Ward, D.E. (1996). Open-path Fourier transform infrared studies of large-scale laboratory biomass fires. Journal of Geophysical Research: Atmospheres, 101, 21067-21080

Table 1. Summary of operational satellite remote sensing fire products.

Satellite	Sensor	Algorithm	Spatial Resolution (at nadir)	Spectral Channel (μm)	Main Output	Day/Night
NOAA-15 NOAA-16 NOAA-17	AVHRR	Fire Identification, Mapping and Monitoring Algorithm (FIMMA)[1]	1 km	3.7, 10.8	Fire pixel geolocation	Day & Night
Terra Aqua	MODIS	MODIS Active Fire[2]	1 km	4, 11	Fire pixel geolocation, surface background temperature, FRP	Day & Night
Suomi NPP	VIIRS	VIIRS M-Band Active Fire[3]	750 m	4, 11	Fire pixel geolocation, FRP	Day & Night
Suomi NPP	VIIRS	VIIRS I-Band Active Fire[4]	375 m	0.64, 0.86, 1.6	Fire pixel geolocation, FRP	Day & Night
Suomi NPP	VIIRS	VIIRS Nightfire[5]	750 m	1.2 1.6, 3.7, 4	Fire pixel geolocation, fire size, fire temperature, surface background temperature, FRP	Night
Meteosat Second Generation (MSG)	SEVIRI	Active Fire Monitoring (FIR)[6]	3 km	3.9, 10.8	Fire pixel geolocation, FRP	Day & Night
GOES-13 GOES-15	GOES Imager	Wildfire Automated Biomass Burning Algorithm (WF-ABBA)[7]	4 km	3.9, 11.2	Fire pixel geolocation, fire temperature, fire size	Day & Night

[1] (Giglio et al. 1999; Li et al. 2001; Li et al. 2000); [2] (Giglio et al. 2003; Giglio et al. 2016; Justice et al. 2002); [3] (Csiszar et al. 2014); [4] (Schroeder et al. 2014); [5] (Elvidge et al. 2013); [6] (Roberts et al. 2005; Roberts and Wooster 2008); [7] (Prins and Menzel 1992, 1994)

Table 2. MODIS land covers reassigned to more general vegetation types as in GFED4.

MODIS Land Cover Type	Clustered Vegetation Type
Evergreen needleleaf forest (ENF)	Tropical, Temperate, Boreal[1]
Evergreen broadleaf forest (EBF)	Tropical, Temperate, Boreal
Deciduous needleleaf forest (DNF)	Tropical, Temperate, Boreal
Deciduous broadleaf forest (DBF)	Tropical, Temperate, Boreal
Mixed forest (MF)	Tropical, Temperate, Boreal
Closed shrublands (Shrub)	Savanna
Open shrublands (Shrub)	Savanna
Woody savannas (Sava)	Savanna
Savannas (Sava)	Savanna
Grasslands (Grass)	Savanna
Croplands (Crop)	Agricultural

[1] If latitude between 30N and 30 S: Tropical, if latitude between 30N/S and 50N/S: Temperate, and if latitude larger than 50N: Boreal

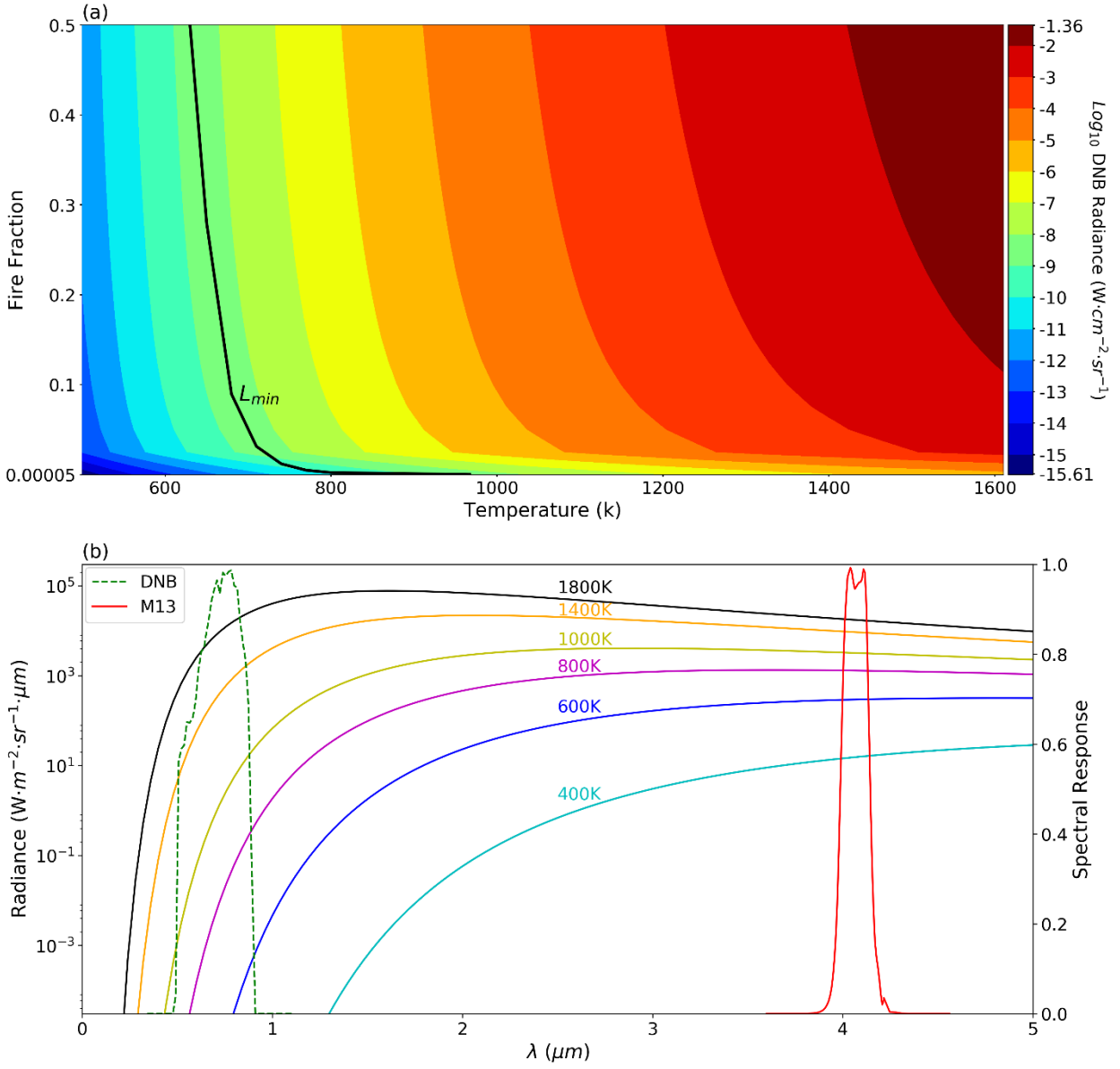

Fig. 1. (a) Contour plot of simulated DNB radiance for different fire temperatures and fractions during nighttime (moon effect is not included) using Unified Linearized Vector Radiative Transfer Model. The black line shows the minimum radiance (L_{min}) that DNB sensor can detect. The fires that fall into the left side of the white line are not detectable by DNB sensor. (b) Plot of VIIRS Day-Night band (DNB) and 4 μm moderate-resolution band #13 (M13) spectral responses along with different Plank curves for different temperatures. DNB is highly sensitive to high temperature (flaming) fires in the night while M13 is sensitive to all fire temperatures.

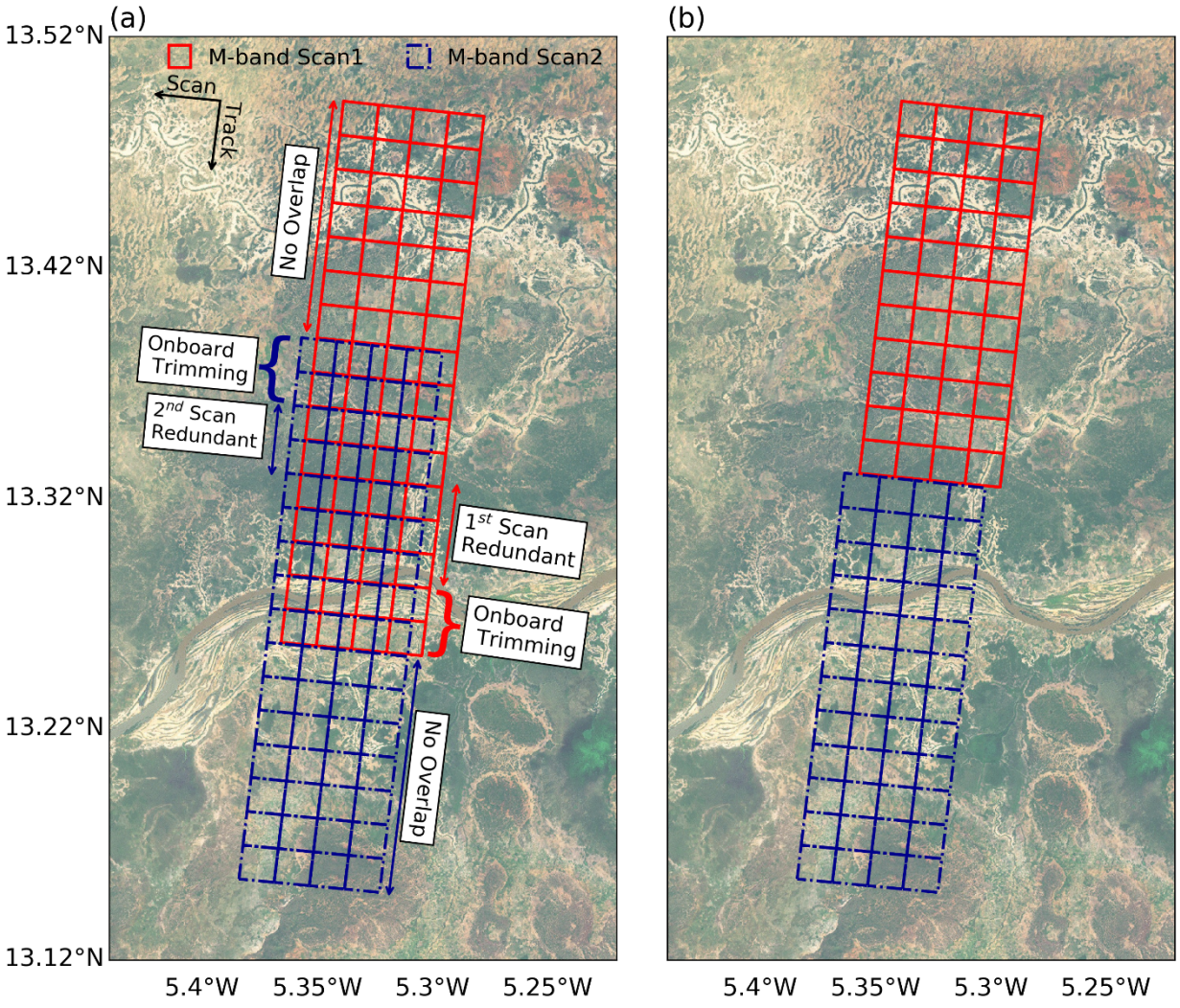

Fig. 2. View of 2 consecutive VIIRS scan zones (at the edge) overpassing Bani River in Africa. (a) Before the bowtie effect correction there are 9 overlapped scan lines from which 4 are trimmed onboard, 2 bottommost Scan1 scan lines and 2 topmost Scan2 scan lines. The other redundant scan lines are detected using respective DNB signals which results in 3 redundant scan lines from Scan2 and 2 from Scan1. (b) Consecutive scan zones after the bowtie effect correction.

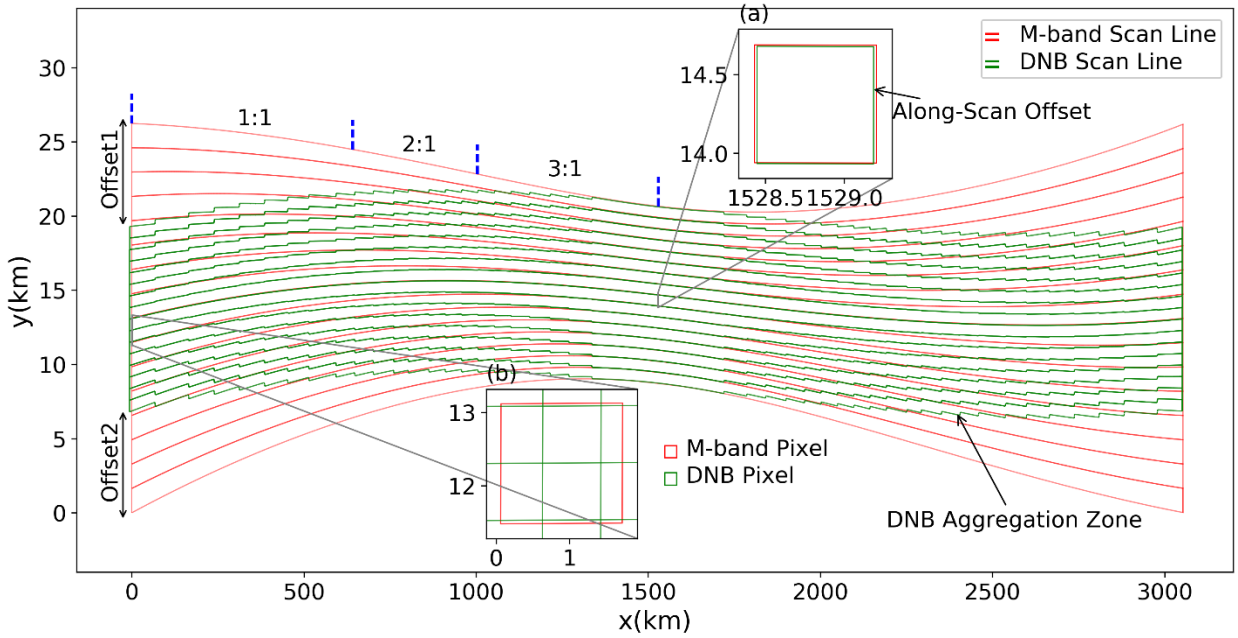

Fig. 3. VIIRS M-band/DNB scan zone for the whole swath projected on a flat plane. The DNB pixels keep the same size throughout the whole scan while the M-band pixel size grows as a function of scan angle. Near the edge, there is an offset (Offset1 & Offset2) of 8 scan lines between DNB and M-band. The bumps in the DNB scan lines indicate beginning of a new DNB aggregation zone with a different number of across-scan aggregated samples than its adjacent aggregation zones which constitutes a collocation segment. Subset. a represents the zoom-in view of the nadir M-band and DNB pixels in which the denoted along-scan empty space between M-band and DNB pixels is due to their nominal spatial resolution mismatch. Subset. b shows the zoom-in layout of the edge M-band and DNB pixels. Each large near-edge M-band pixel can overlap with up to 12 DNB pixels from 4 different DNB scan lines. Note, the different scales for X and Y axes makes the figure exaggeratedly look curvy.

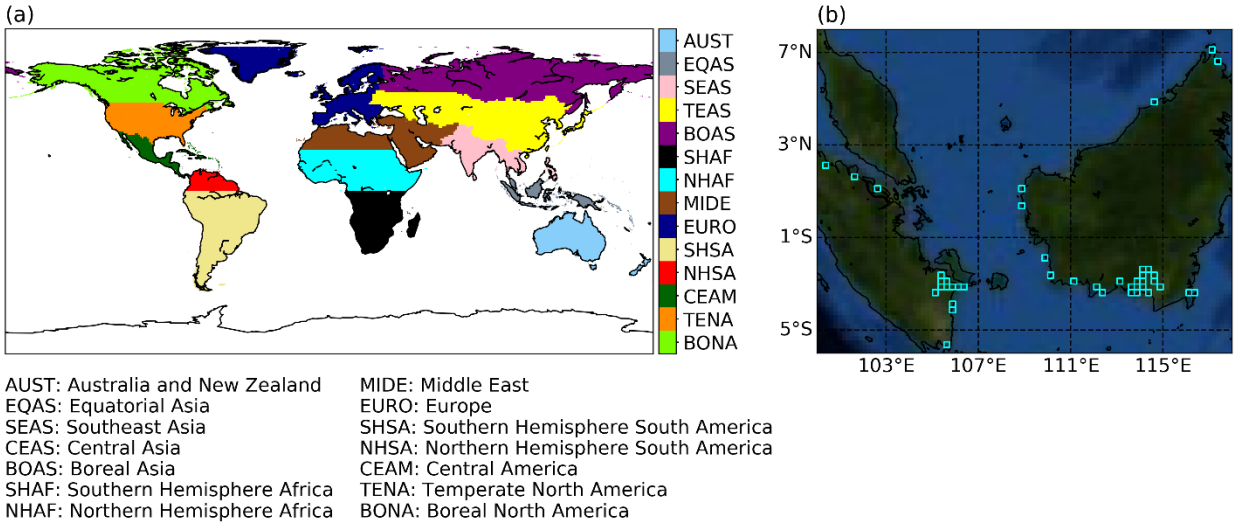

Fig. 4. (a) Map of 14 basic regions used by GFED. (b) Peatland locations in cyan-colored boxes used in this study. Each grid land cover is comprised mostly from peats (70%). The background base map is from ESRI (Environmental Systems Research Institute) world imagery service.

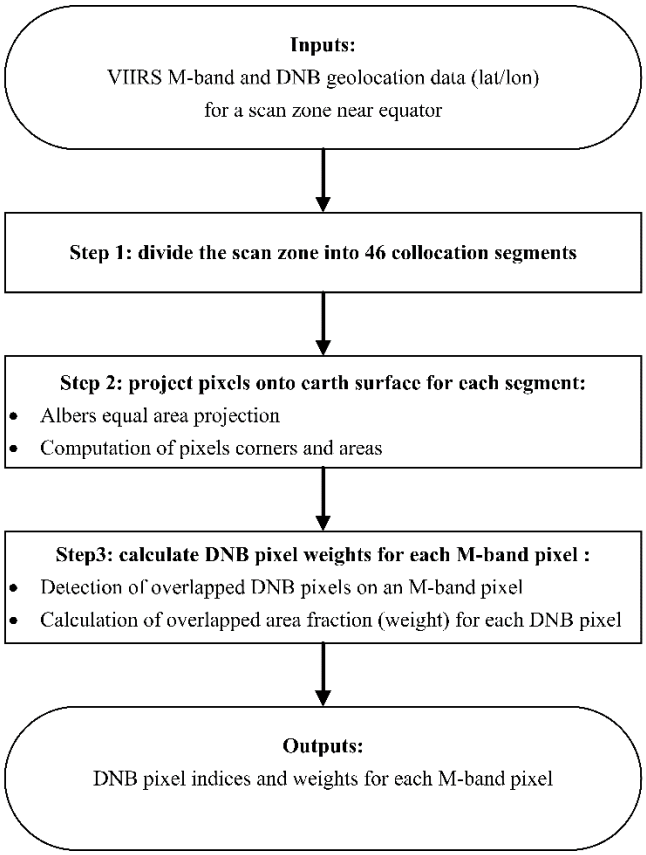

Fig. 5. Flowchart demonstrating the collocation process.

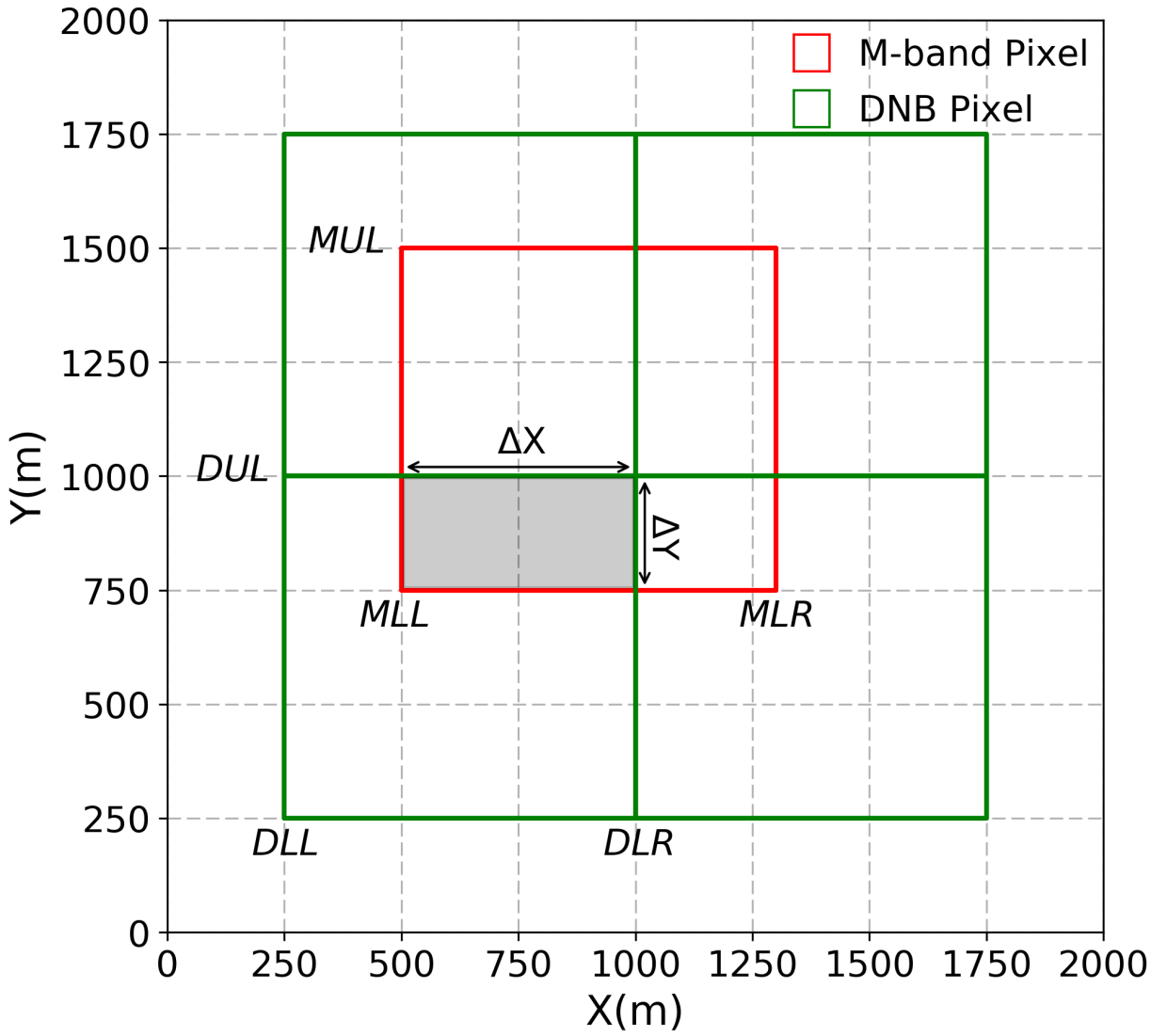

Fig. 6. Detecting intersection area between M-band and DNB pixel. The two pixels are overlapped if $(x_{DLR} - x_{MLL})$ and $(y_{DUL} - y_{MLL})$ are simultaneously larger than zero. Subscripts of *DLL*, *DLR*, *DUL*, *MLL*, *MLR*, and *MUL* stand for DNB lower left, DNB lower right, DNB upper left, M-band lower left, M-band lower right, and M-band upper left respectively. The X axis corresponds to projected longitudes while Y axes represent projected latitudes.

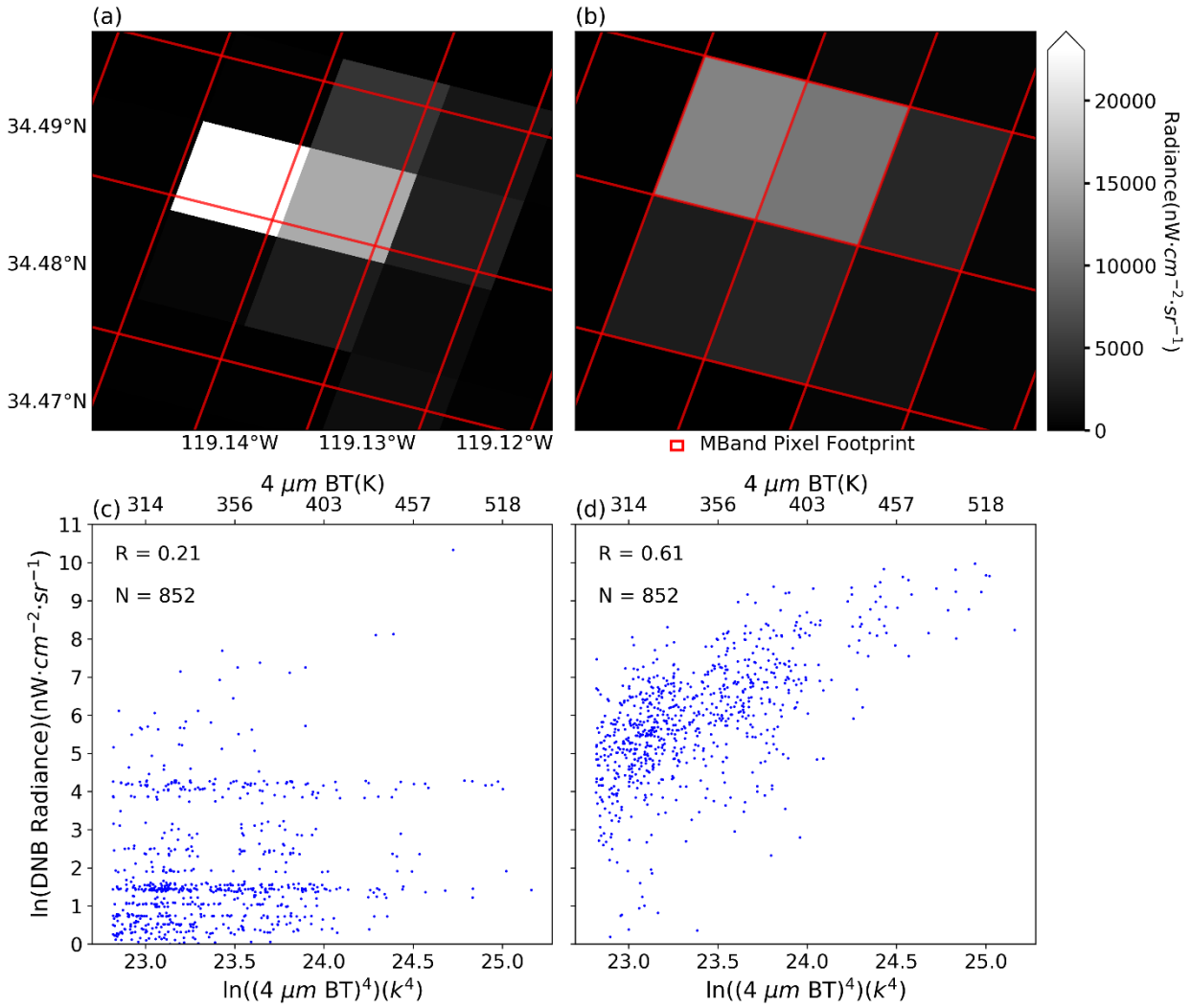

Fig. 7. An example of resampling nighttime DNB pixels radiances to M-band pixels using collocation LUT method for Thomas wildfire on December 12, 2017. (a) Zoom-in view of the original DNB radiances (bright squares) before the collocation. (b) The DNB radiances after collocation to the M-band footprint (red rectangles). (c) Scatter plot of BT_4^4 and collocated DNB radiances for VIIRS AF (nighttime) fire pixels (Thomas wildfire) during the December 5 to January 12, 2017 period when only the nearest DNB pixels in each scan line are collocated to the M-band pixel footprint without considering the across-scan offset. The low correlation coefficient indicates the low accuracy of the nearest-neighbor collocation method. (d) Same as Fig. 7c, but here the collocation LUT method results in a high correlation between the collocated DNB radiances (both across and along the scan) and the corresponding M-band pixel BT_4^4 values.

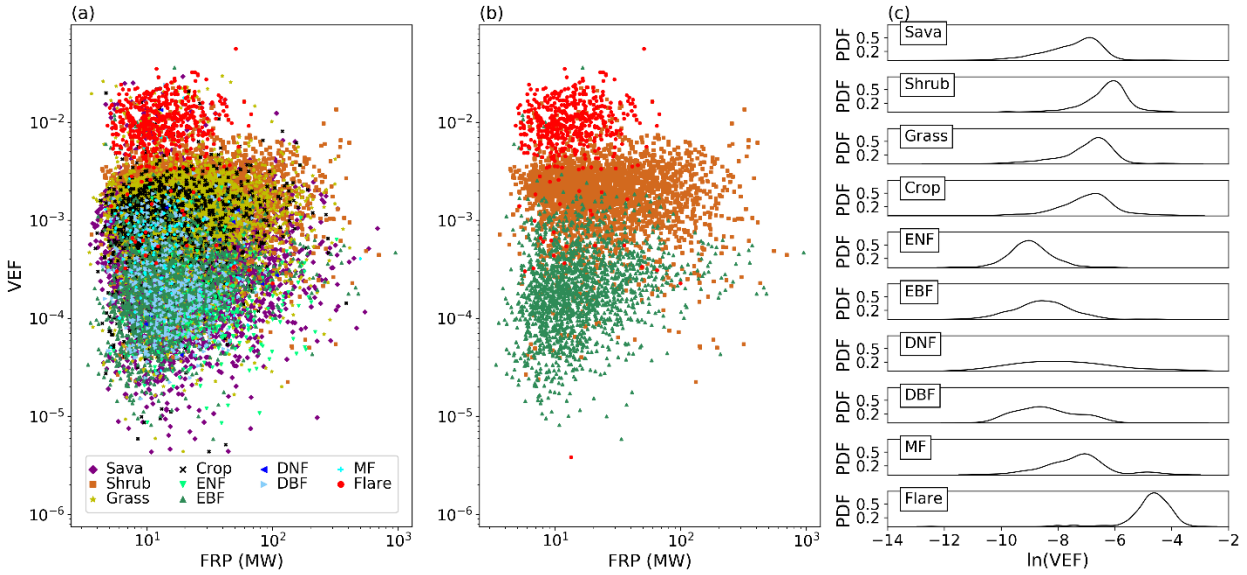

Fig. 8. (a) Scatter plot of different fire types VEF and FRP values. The fire types are based on the different vegetation types (Table 2) plus gas flares. Each point on the scatter plot represent a 0.05˚ grid average VEF (y-axis) and FRP (x-axis) values for 2017 (only nighttime). Different fire types are clustered by their VEF value ranges while they have a similar FRP range. (b) Same as Fig. 9a, but here only three fire types are presented for better visualization. Gas flares have the highest VEF range while EBF has the lowest VEF clustered under the shrublands. (c) The probability density functions (PDF) for different vegetation types showing their VEF distribution for the year 2017. Sava, shrub, grass, and crop ln(VEF) values are mostly distributed from -8 to -5 while different forest types are from -10 to -7 and gas flares are mostly spread in the highest range from -6 to -3.

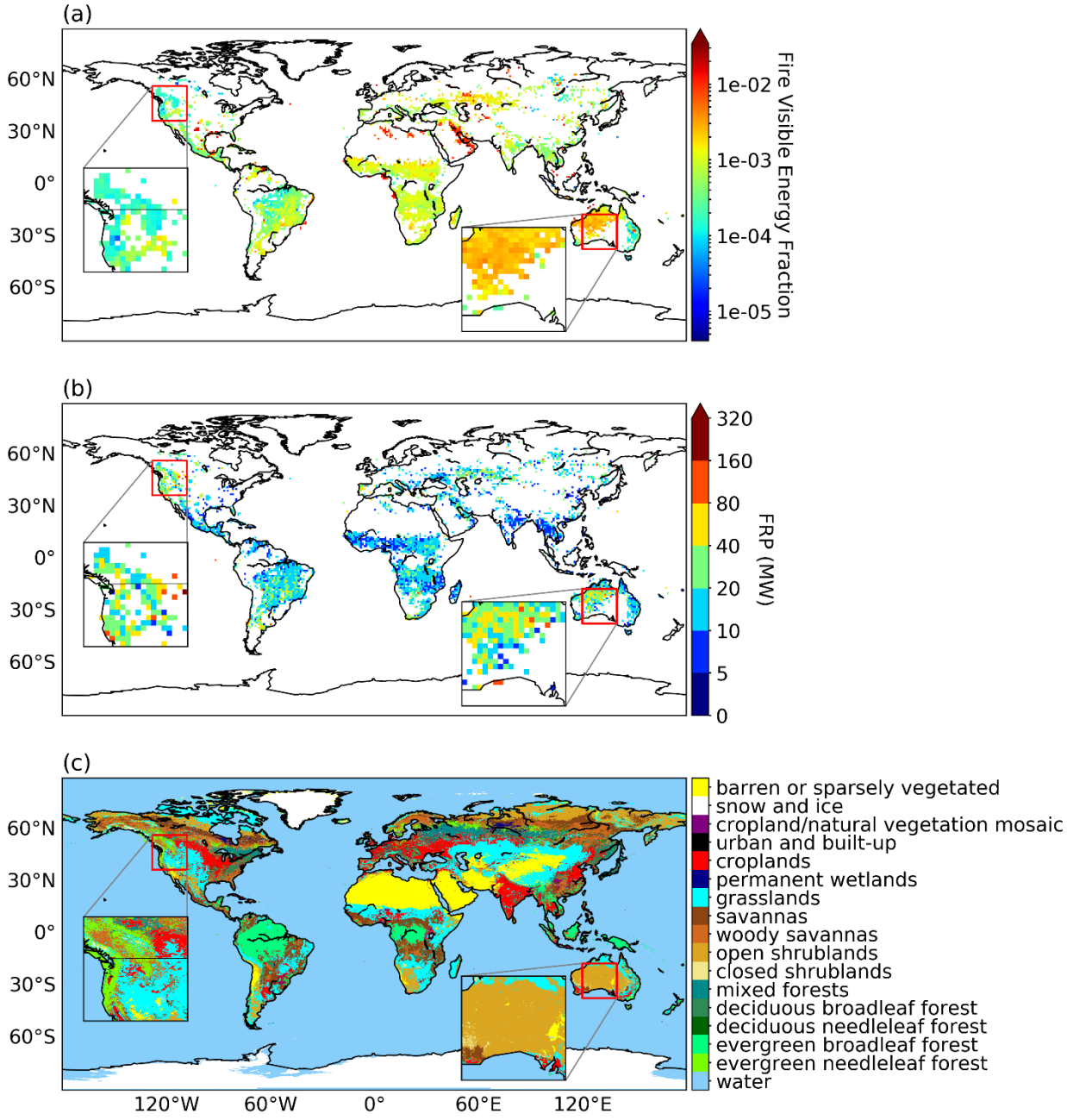

Fig. 9. (a) Global map of VEF for 2017. Each 1˚ grid represents the average VEF value for the year 2017. The VEF map shows the transition from forest land cover type in North America (lower VEF) to shrublands in Australia (higher VEF). The red grids (highest VEF) are mostly corresponding to the gas flares while the lowest VEF (blue color) are where the evergreen forests are. There are no detected nighttime fire pixels in polar regions including Greenland and Alaska due to the long day length (more than 20 hours) during their fire seasons in summer. (b) Global map of FRP for 2017. Each 1˚ grid represents the average nighttime FRP value for the year 2017. The FRP map is not capturing the fire combustion phase differences based on the land cover type as the FRP spread for shrubland and forest are similar. (c) Global landcover map generated based

on the MODIS Land Cover Type Climate Modeling Grid for the year 2017. The land cover categories are according to IGBP scheme.

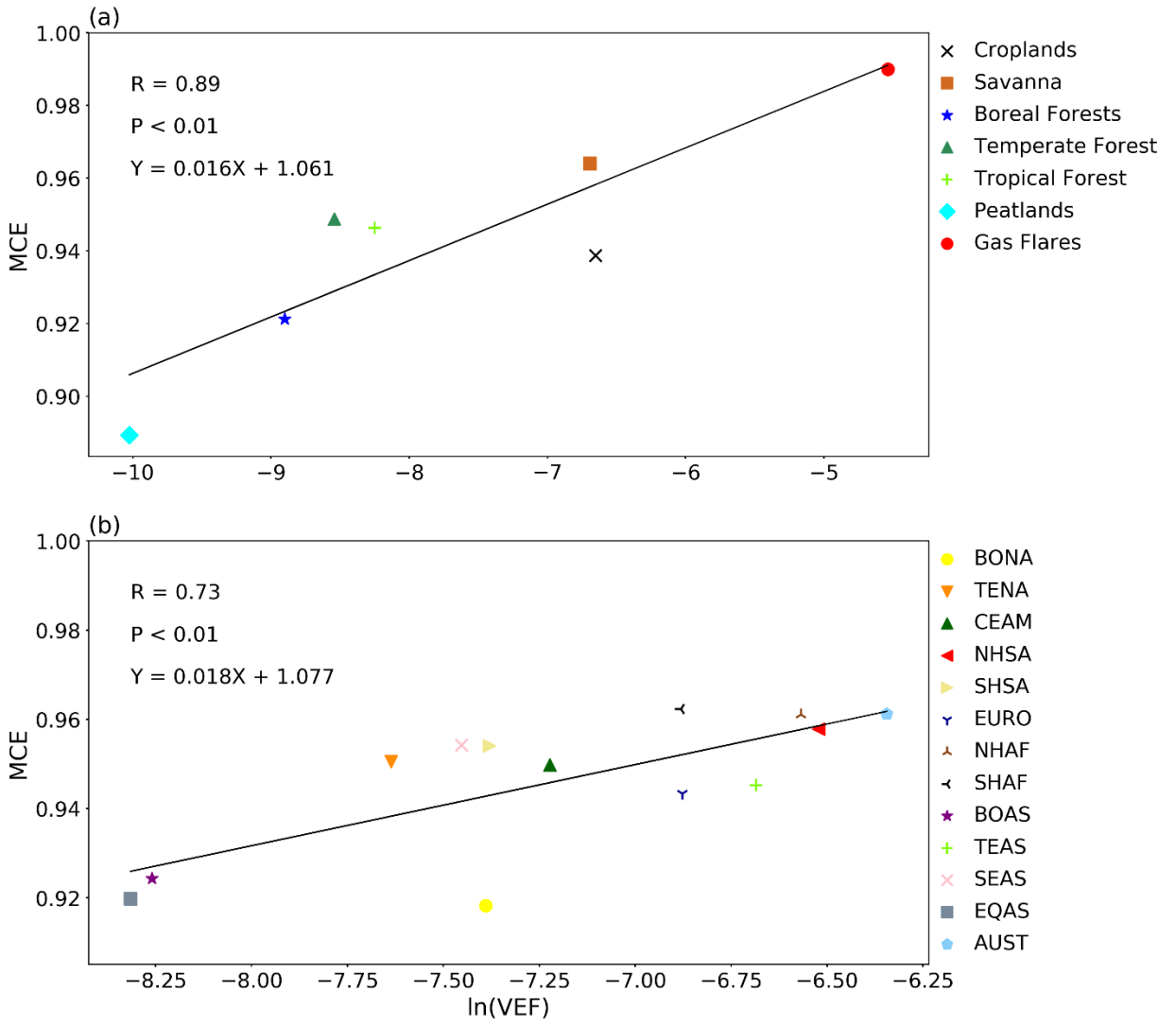

Fig. 10. (a) Scatter plot of annual-averaged (2017) GFED4 MCE and ln(VEF) for different biomes. Correlation coefficient is 0.92 indicating VEF is a successful indicator of fire combustion phase for different biomes. (b) Scatter plot representing the regional MCE and VEF relationship. Each point represents GFED4 MCE (y-axis) and the natural logarithm of VEF (x-axis) averaged for a GFED4 basic region during 2015.

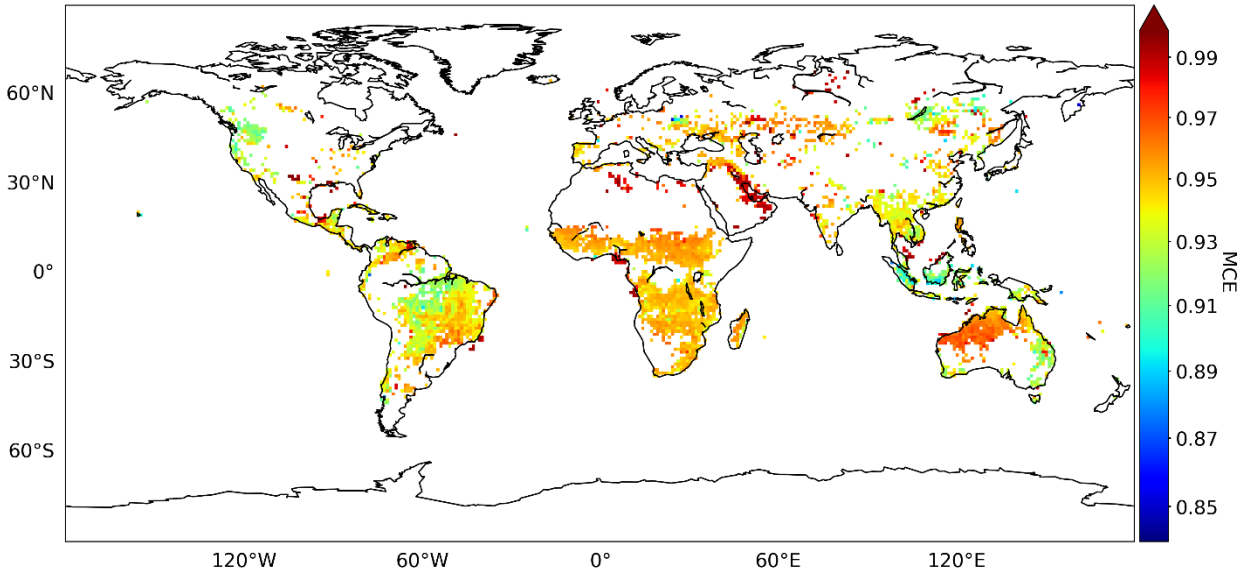

Fig. 11. Global map of MCE for each 1˚ grid which are calculated based on their VEF values for2015. The Australia shrublands have a high MCE while the forest land cover type areas represent low MCE. The gas flares have the highest MCE.

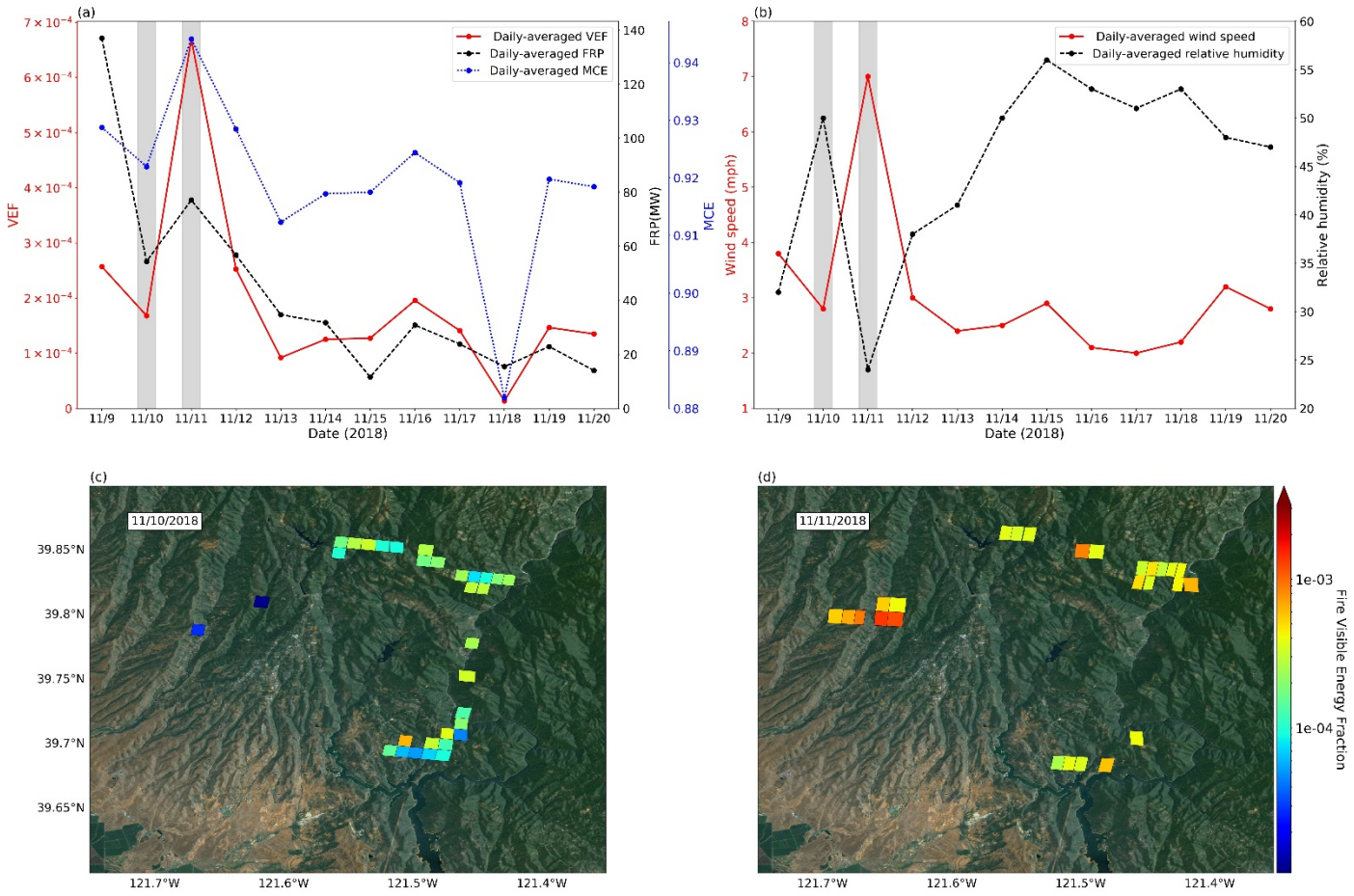

Fig. 12. (a) Time series of FRP (black dashed line), VEF (red solid line), and MCE (blue dashed line), which was calculated based on equation 9, for the nighttime fire pixels. November 11, 2018 is the peak in the VEF indicating of highly flaming fire phase. (b) Time series of wind speed (red solid line) and relative humidity (black dashed line) during Camp Fire. These data are obtained from Openshaw station from Raws network. (c) Observation of Camp Fire intensity on November 10, 2018 when most the fire pixels are in an early stage of their lifetime. (d) Fire intensity increases comparing to the previous day as the fire reaches to a flaming phase on November 11, 2018. Note, the fire pixels for these two days are extracted only from one satellite orbit observation in that day. The background base map is from ESRI (Environmental Systems Research Institute) world imagery service.